Progress report

PROJECT P3VENTI – PROGRAM LINE 2
(project phase 2022)

TU/e

**EINDHOVEN
UNIVERSITY OF
TECHNOLOGY**

Date	Our reference	Version
30 January 2023	BE2023/1972728	1.0

Authors
Luyang Kang
Marcel Loomans
Twan van Hoof

Contents

1. Introduction

The research program *Pandemic Preparedness and Ventilation* (*P₃VENTI*) was initiated to develop knowledge on the role of airborne spread (aerogenic route) of viruses and other pathogens, to increase the effectiveness of using ventilation as a mitigation measure and to develop methods and tools to support government and social partners in often complex and sensitive decision making. The knowledge developed has application in society in mind.

For research into the spread of virus particles and other pathogens in a room, computational fluid dynamics (CFD) is an important tool. It can provide high-resolution whole-flow field data on the relevant parameters in space, allows us to evaluate the exposure to pathogens in controlled situations, and investigate the effect of interventions in the design phase.

However, modeling will always require some degree of simplification of the complex world. This also accounts for CFD. The context of modeling airborne spread of pathogens introduces extra requirements besides the mere modeling of the airflow (velocity and temperature). In this first phase of Program Line (PL) II, which focuses on modeling and simulation using CFD, we investigated some important aspects related to modeling the spread of virus particles. This research allows for better-grounded decisions with respect to the modeling of such spread for realistic situations. The analysis is based on defined performance indicators that are regarded feasible for the assessment of the spread.

For the research in 2022, three sub-studies have been executed (*Activiteiten 2.1-2.3*). Each sub-study deals with an important aspect of the modeling of air flows in rooms, but specifically also with aspects that are directly related to the modeling of the pathogens and their spread.

Firstly (*Activiteit 2.1*), it is investigated whether the behavior of (viral) particles can be modeled sufficiently accurate in a simplified manner via the Eulerian approach, instead of a Lagrangian approach. The Eulerian approach is a much simpler means to model the spread of particles as compared to the Lagrangian approach. The Eulerian approach has some options to include the gravitational force that acts on particles, the so-called drift-flux model. This model has been included in the analysis

Next (*Activiteit 2.2*), it is investigated how the emission of (virus) particles, via human respiration, can be modeled best. Here the question is whether there is a need to model the complex sinusoidal breathing rhythm to assess the exposure in the room. The complex breathing rhythm would require extensive transient simulations, which will be much more time-consuming than steady-state simulations that can be applied when assuming a constant exhalation of particles/aerosols. Here, it will be important to assess how the performance indicators are affected by the change in breathing modeling.

Finally (*Activiteit 2.3*), the effect of motion on airflow is considered. The question here is to understand whether there is a need to model (human) movement and how to model that best. Dynamic mesh solutions are available, but it is not realistic to apply such solutions in case many situations need to be investigated. Alternative options, via (momentum) sources have been investigated. In addition, the question may be asked what the effect of movement is on the total exposure, when the airflow may be assumed undisturbed for longer periods of time.

As can be read from the above introduction, the ultimate goal is to keep the modeling of the mentioned components as simple as possible, without affecting the important performance indicators that are being assessed. With this information, we hope to serve the overall objective for this PL: Detailed modeling of particle distribution and particle concentrations in realistic rooms, taking into account realistic emission patterns, human presence and behavior and ventilation equipment characteristics.

In summary, the aim of the first phase within PLII is to make an inventory of the numerical modeling of exposure to virus particles in order to further detail the follow-up research within this PL. For this phase, CFD simulations in combination with a literature study have been conducted to answer the following three questions:

1) Whether the behavior of virus-laden particles can be modeled sufficiently accurately in a simplified manner via the Eulerian approach instead of a Lagrangian approach?
2) How can the emission of virus-laden particles via human respiration best be modeled?
3) How to take into account the effects of human movement on the airflow in an efficient way in the modeling?

These topics have been defined as individual deliverables (D2.1-D2.3) within program line II for 2022. However, due to the close connection between the research questions, we grouped the research and its outcomes in one report. The general method for the sub-studies uses literature for defining cases that can be used to validate and compare the outcomes from the CFD analyses. The details of that will be described further below. We will end the report with an overall conclusion and practical implications for the remainder of the program and specifically for PLII. This refers to *Activiteit 3.1* and *Deliverable 3.1* as described in the PLII for 2022.

2. General background

2.1. Modeling approach of particle dispersion

Generally, there are two main approaches to modeling particle transport in CFD simulations, the Eulerian-Eulerian approach (hereafter referred to Eulerian approach) and the Eulerian-Lagrangian approach (hereafter referred to Lagrangian approach) (e.g. Zhao et al., 2004a,b,c; Gao and Niu, 2007; Lai and Chen, 2007; Zhang and Chen, 2007; Zhao et al., 2008). The Eulerian approach treats the particle phase as a continuum and develops its conservation equations based on a control volume. On the other hand, the Lagrangian approach considers particles as a discrete phase and tracks the pathway of each individual particle (e.g. Zhang and Chen, 2007; Li et al., 2022c). Many past studies indicated that the size of human exhaled droplets in close proximity to the mouths is in the super-micrometer size (e.g., Chen and Zhao, 2010). The particle size during a human breathing process is usually smaller than 10 µm (Asadi et al., 2019), which makes it possible to use the passive scalar approach, one form of the Eulerian approach, to model the human exhaled particle dispersion. However, the gravitational effect of large particles cannot be neglected. Therefore, another form of the Eulerian approach is adopted in the modeling of airborne transmission of human exhaled particles, i.e., the drift-flux model. The term drift flux stands for particle flux caused by effect other than convection, i.e., gravitational settling (Lai and Chen, 2007).

For this project, two numerical models based on the Eulerian approach, and one model of the Lagrangian approach will be tested to find the most efficient way to model particle dispersion and deposition from human breathing. To make a brief explanation, these three models are:

- Passive scalar (Eulerian model): solves the standard species transfer governing equation. Passive scalar is a diffusive contaminant in a fluid flow that is present in low concentrations and that has no dynamic effect on the fluid motion itself (Warhaft, 2000).

- Drift flux (Eulerian model): integrates the gravitational settling effect of particles into the governing equation of the standard species transfer (Chen et al., 2006).
- Lagrangian: tracks the trajectory of each particle by solving the force balance equations of particle movement (Wang and Chow, 2011).

2.2. Human breathing mode

Based on human subject studies, the human breathing rate takes an approximately sinusoidal form (Gupta et al., 2010). Transient simulations should be performed to capture the dynamic features of the human periodic breathing cycle, which undoubtedly adds to the computational cost. Therefore, a steady simulation has the potential to provide reliable simulation results in an economical way. As Ai and Melikov (2018) reported, the most widely investigated breathing mode in previous studies, for both the infected and exposed individual, was exhalation through the mouth and inhalation through the nose (e.g. Qian et al., 2006; Olmedo et al., 2013; Villafruela et al., 2016). A number of studies were carried out using the "non-breathing" mode for the exposed manikin (e.g. Lipczynska et al., 2015; Yang et al., 2015).

To find an efficient way in modeling particle emission of human breath, one transient breathing mode and two steady breathing modes are numerically examined in this project.

2.3. Modeling approach to human movement

Locally, the air movements created by a moving person can overwhelm that person's body thermal plumes when the walking speed is above 0.2 m/s (Edge et al., 2005). They can also easily break down the stratification of the expiratory flow and the convective boundary layer (CBL) around a nearby person (Bjørn and Nielsen, 2002). In general, a walking person enhances air mixing in the whole room, which could result in unexpected spread of airborne pollutants (Brohus et al., 2008).

The dynamic mesh method is commonly applied in modeling human movement (Wang and Chow, 2011; Cao et al., 2017; Eslami et al., 2017; Mei et al., 2019), which means the computational grid is updated at each time step. This significantly increases the simulation complexity and the computational time. There are other economical methods for modeling human movement, e.g., immersed boundary method (Choi and Edwards, 2008), sliding mesh method (Han et al., 2014; Al Assaad et al., 2019), or momentum source method (Brohus et al., 2008; Cao et al., 2017).

To find a simple method to model human movement, the two modeling methods, i.e., the overset mesh method and the momentum source method, are numerically tested in this project.

2.4. Performance indicators

To quantify the risk of cross-infection and ventilation efficiency in contamination removal, many performance indicators can be found in the literature, e.g., intake fraction (Nazaroff, 2008), exposure index (Villafruela et al., 2016), infection risk (Wells-Riley model) (Sze To and Chao, 2010), reproductive number (Cermak and Melikov, 2007), effectiveness of contamination removal (Cao et al., 2014) and air change efficiency (Villafruela et al., 2013a). Among all these performance indicators, the concentration and the normalized concentration in the inhaled airflow of an exposed individual were most commonly used as an indicator of infection risk (Ai and Melikov, 2018). On the other hand, ventilation efficiency in contamination removal only presents the overall performance of a ventilation system, which is not directly related to the risk of cross-infection and thus is not discussed in this report. Herein, two performance indicators commonly

used in the study of airborne transmission of exhaled pollutants are described, which can be used to assess the results from the CFD simulations for different scenarios.

2.4.1. Intake fraction

Intake fraction is defined as the proportion of exhaled pollutant mass from the infected individual that is inhaled by the exposed individual (Nazaroff, 2008; Ai and Melikov, 2018). The intake fraction (IF) can be expressed as:

$$IF(t) = \frac{C_{in}M_{in}}{C_{ex}M_{ex}} = \frac{\int_0^{t_{in}} C_{in}(t)M_{in}dt}{\int_0^{t_{ex}} C_{ex}(t)M_{ex}dt} \tag{1}$$

where C_{in} is the inhaled pollutant concentration of the exposed individual, which can be calculated based on the product of the average concentration at the nose surface/breathing zone and the inhalation velocity; C_{ex} the exhaled pollutant concentration of the infected individual; M_{in} and M_{ex} mass flow rates of inhaled airflow of the exposed individual and exhaled airflow of the infected individual, respectively; $C_{in}(t)$ and $C_{ex}(t)$ the inhaled pollutant concentration of the exposed individual and the exhaled pollutant concentration of the infected individual at time t, respectively; t_{in} and t_{ex} the exposure time of the exposed individual and the release time of the infected individual, respectively.

2.4.2. Exposure risk

Unlike the intake fraction (IF), the exposure index takes the concentration at the ventilation exhaust, instead of at the source person, as a normalization reference to indicate the risk of cross-infection of the exposed person, which can be expressed as (Ai et al., 2019):

$$\overline{\varepsilon_s(t)} = \frac{\overline{C_{in}(t) - C_{supply}(t)}}{C_{exhaust}(t) - C_{supply}(t)} \tag{2}$$

where C_{in} is the inhaled pollutant concentration of the exposed individual, C_{supply} and $C_{exhaust}$ are the pollutant concentration at the ventilation supply and exhaust, respectively; the overhead bar indicates averaging during the time period of t. For steady state, when the supply air is totally clean, i.e., $C_{supply}(t) = 0$, the exposure risk can be rewritten as:

$$\varepsilon_s = \frac{C_{in}}{C_{exhaust}} \tag{3}$$

The steady-state exposure risk was extensively used in many numerical and experimental studies (e.g., Olmedo et al., 2012, 2013; Villafruela et al., 2013a; Villafruela et al., 2016). Apart from inhaled pollutant concentration of the exposed individual, concentration in the occupied zone or breathing zone is also used to calculate the exposure risk.

In order to obtain a proper evaluation of dynamic airborne transmission, another evaluation method was developed for the exposure risk (Ai et al., 2019). This method utilizes the stability of the average concentration at the ventilation exhaust under steady-state conditions. The improved indicators are called real-time risk of cross-infection at a specific moment and average risk of cross-infection during a particular period of time (since the start of the event), respectively:

$$\varepsilon_d(t) = \frac{C_{in}(t)}{C_{exhaust-steady}} \tag{4}$$

$$\overline{\varepsilon_d(t)} = \frac{\overline{C_{in}(t)}}{\overline{C_{exhaust-steady}}}$$

(5)

where $\varepsilon_d(t)$ and $\overline{\varepsilon_d(t)}$ are the real-time exposure index and the time-averaged exposure index, respectively; $\overline{C_{exhaust-steady}}$ is the average concentration at the ventilation exhaust under steady-state conditions. The above dynamic exposure risks were used in several studies on the short-term airborne transmission of inhaled pollutants (Ai et al., 2019; Li et al., 2022a, 2022b).

3. Modeling of particles (Eulerian versus Lagrangian)

The drift-flux model, which integrates the gravitational settling effects of particles into the concentration equation, was adopted for the Eulerian approach. A detailed description of the governing equations of this model can be found in Chen et al. (2006) and Zhao et al. (2008). Due to the small particle size, the interaction between the fluid and the particles was treated as one-way coupling in the Eulerian simulation. For the Lagrangian simulation, the discrete random walk (DRW) model was used. The interaction between air and particles was included.

3.1. Computational geometry and grid

Detailed experimental data on the distributions of velocity and particle concentration (10 µm) were provided by Chen et al. (2006) for a small experimental chamber (Figure 1). This benchmark experiment is used here to validate the accuracy of Eulerian and Lagrangian modeling approaches. The chamber has dimensions of 0.8×0.4×0.4 m³ (L×H×W). A rectangular opening size (0.04×0.04 m²) was adopted both for the inlet and the exhaust. A structured grid with a high spatial resolution near the surfaces was created, as shown in Figure 2 and Figure 3a. The total cell number was 187,500.

3.2. Boundary conditions and solver settings

The particle density was 1400 kg/m³, and the inlet velocity was 0.225 m/s (Chen et al., 2006). For Eulerian simulation, deposition flux was calculated and added to the floor surface (Lai and Nazaroff, 2000; Zhao et al., 2004a). For the Lagrangian simulation, the drag force was included and followed the Stokes drag law. Other forces were not included in the simulation. A trap boundary condition for particle tracking was applied on the floor, and on other surfaces a reflective boundary condition was used. A uniform particle injection normal to the inlet was applied with an initial particle releasing velocity of 0.225 m/s.

The simulations were performed using the SST k-ω turbulence model (Menter, 1994). The maximum dimensionless wall distance (y∗) was 3.16, which was lower than 5, enabling the use of low-Reynolds number modeling in the near-wall regions. All transport equations were discretized using a second-order upwind scheme, and second-order pressure interpolation was used. The pressure-velocity coupling was solved using the SIMPLE algorithm. In the Lagrangian simulation, DRM was applied for stochastic tracking, and the tracking scheme was based on the implicit and trapezoidal schemes. A transient simulation was performed for the Lagrangian simulation. A time step of 1 s was selected, and the maximum iterations per time step were 10.

The first 18000 s (300 min) of the transient simulation were discarded. Then the statistical sampling was conducted for 3600 s (60 min).
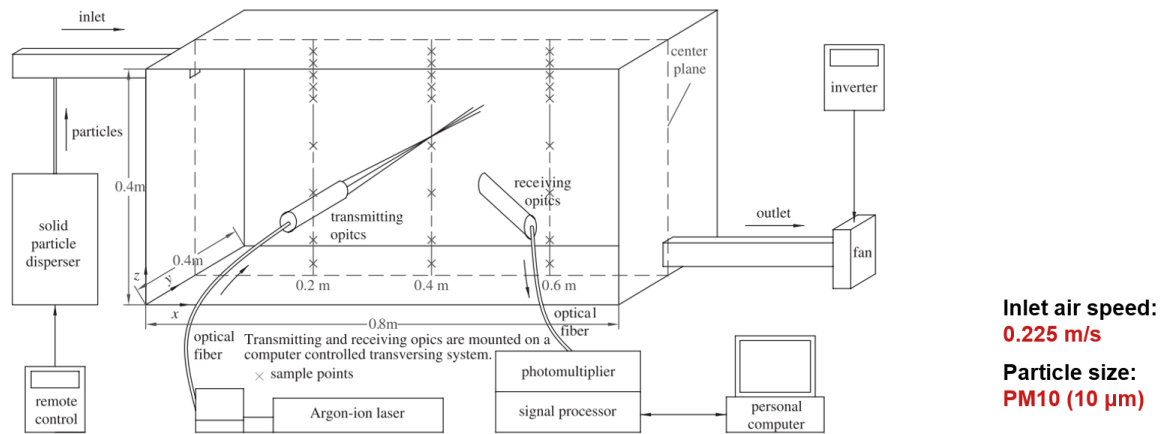

Inlet air speed:
0.225 m/s

Particle size:
PM10 (10 μm)

Figure 1. The benchmark experiment conducted by Chen et al. (2006) for particle dispersion and deposition in a ventilation chamber ($d_p = 10$ μm).

3.3. Results and discussion

Figure 2 compares the velocity component in the X-direction obtained from CFD simulation and experiment. The X-velocity is well predicted in the CFD simulation, which ensures that the flow field is not or hardly affecting the comparison of concentrations.
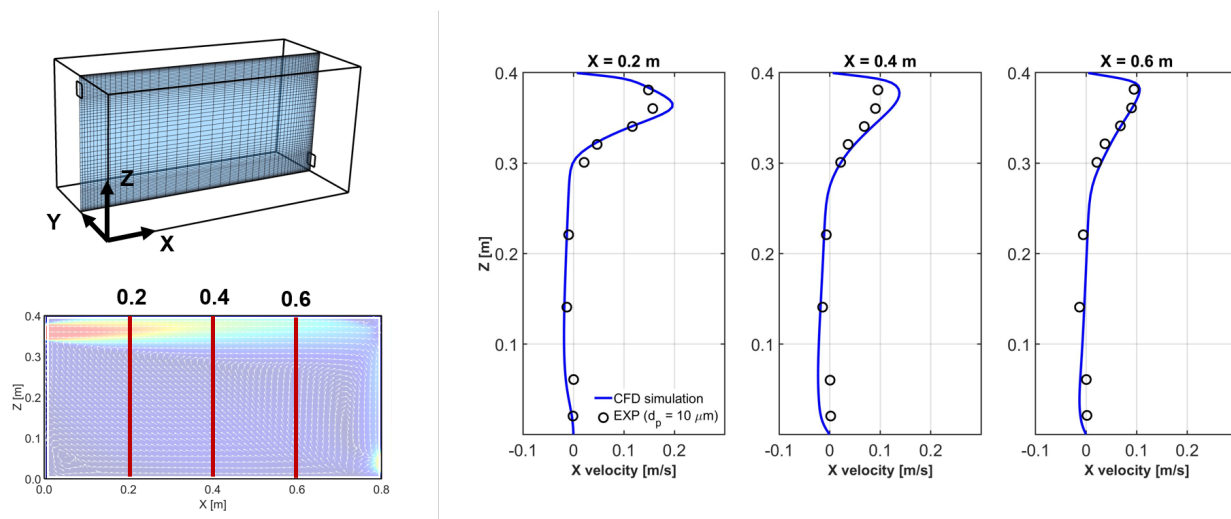

Figure 2. Comparison of X-velocity along three vertical lines in the middle plane obtained with CFD simulation and with experiment.

Title
Progress report

Version
1.0

Page
8 of 41

Figure 3 shows the distributions of velocity and particle concentration (d_p = 10 µm) in the vertical central plane of the ventilated chamber, in which the particle concentration is normalized by the average inlet particle concentration (C/C_{inlet}). Normal to the inlet opening and near the exhaust, the air speeds are relatively high (Figure 3a). In other regions, the air speed is lower than 0.1 m/s. A small secondary recirculation region forms at the bottom left corner of the vertical central plane. For particle concentration, similar distributions are obtained from the Lagrangian modeling approach and the Eulerian modeling approach (drift-flux model), as shown in Figure 3c and Figure 3d. However, below the jet core region (at X ≈ 0.2 m), the dimensionless particle concentration (C/C_{inlet}) from the Lagrangian simulation is slightly higher than that from the Eulerian simulation.

Figure 4 shows that both the Lagrangian discrete random walk (DRW) model and the Eulerian drift-flux model can predict particle dispersion and deposition (for PM10) very well compared to the experimental results. The particle diameter of 10 µm is at the high end for analysis of typical virus-laden particle dispersion in the room (Johnson and Morawska, 2009; Morawska et al., 2009; Ai and Melikov, 2018). For smaller particles, the gravitational effect is weaker. Therefore, based on the validation for PM10, the drift-flux model is suitable for the simulation of typical virus-laden particle dispersion in the room.
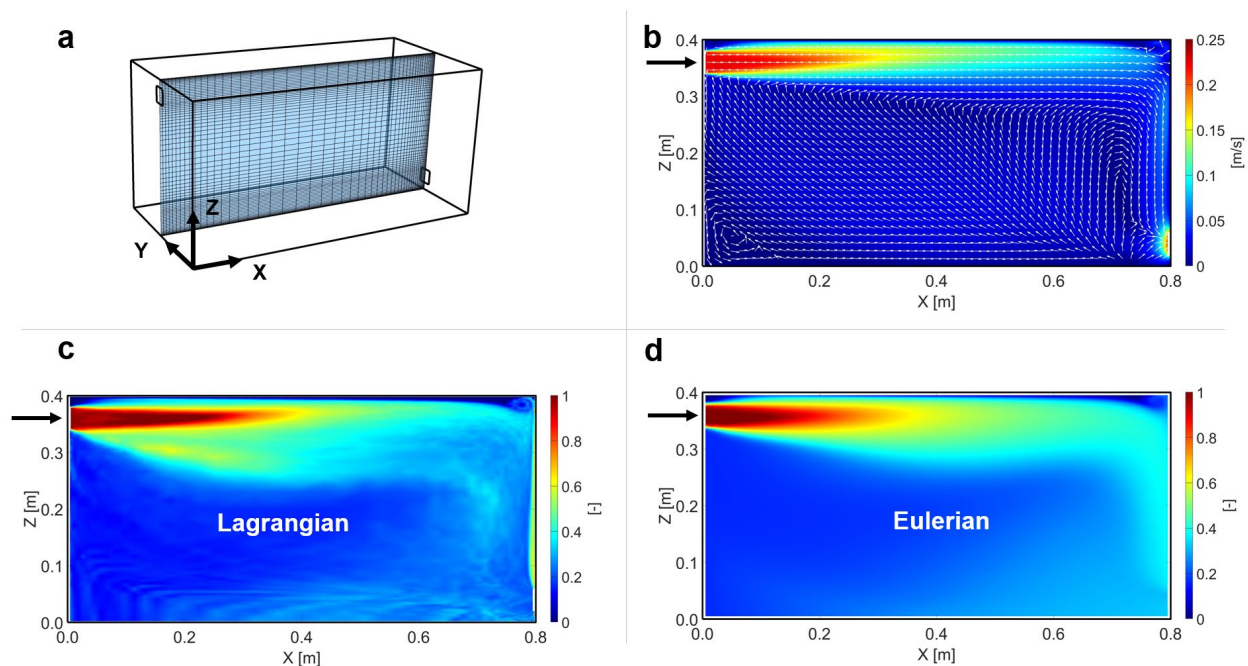

Figure 3. Distribution of air velocity and particle concentration in the middle plane of the ventilation chamber. (a) Computational geometry and grid. (b) Velocity magnitude and velocity vector. (c-d) Dimensionless particle concentration (PM10): (c) Lagrangian approach. (d) Eulerian approach (drift-flux model).
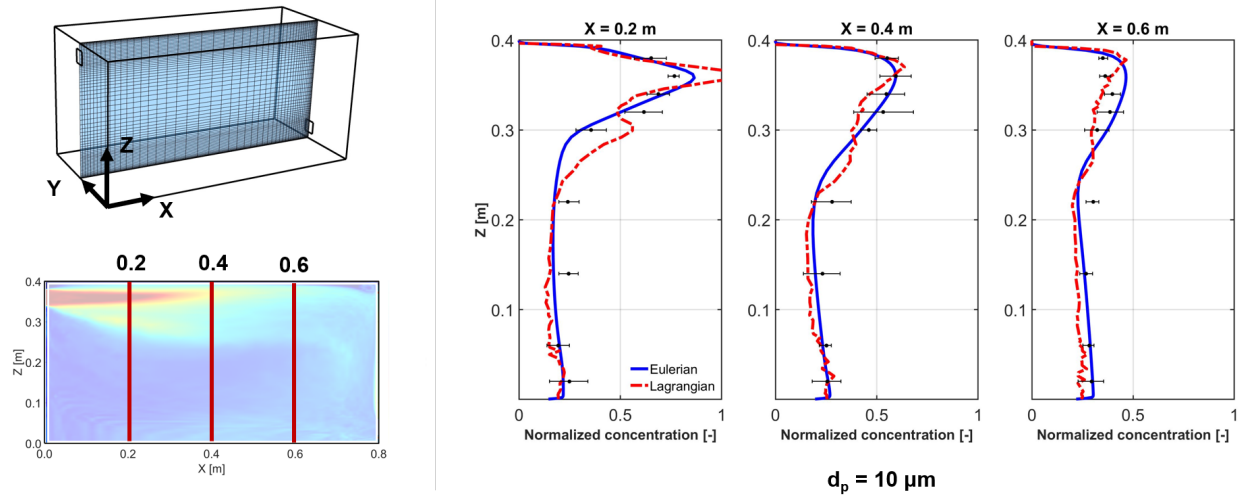
Figure 4. Comparison of dimensionless particle concentration along three vertical lines in the middle plane obtained with Lagrangian approach, Eulerian approach and with experiment.

3.4. Impact of particle size

When using the drift-flux model, only one specific particle size can be used for one scalar. Therefore, in this section, the simulation results for five different particle sizes were investigated in the same ventilated chamber. The studied particle sizes are 0.5 µm, 1 µm, 2 µm, 5 µm and 10 µm.

3.4.1. Particle settling velocity

By equating the drag force with the weight of the particle, i.e., the Stokes flow equation, the terminal settling velocity of a spherical particle can be obtained from the following equation (Finlay, 2001):

$$V_s = \frac{C_c \rho_p g d^2}{18 \mu} \tag{6}$$

where V_s is the particle settling velocity; C_c is the Cunningham slip factor; ρ_p is the particle density; g is the gravitational acceleration; d is the particle diameter; μ is the dynamic viscosity of air.

In order to use the Stokes flow solution for flow past a sphere, there is a restriction on the particle Reynolds number (Re << 1). The particle Reynolds number can be calculated from the following equation:

$$Re = \frac{V_s d}{\nu} \tag{7}$$

Here, ν is the kinematic viscosity of the fluid surrounding the particle.

Figure 5 shows the impact of particle size on the particle Reynolds number and the particle settling velocity. Most inhaled pharmaceutical aerosols readily satisfy the condition that the particle Reynolds number is much smaller than one, as shown in Figure 5a. Furthermore, Table 1 lists the particle Reynolds number and the settling velocities for typical particles investigated in this section
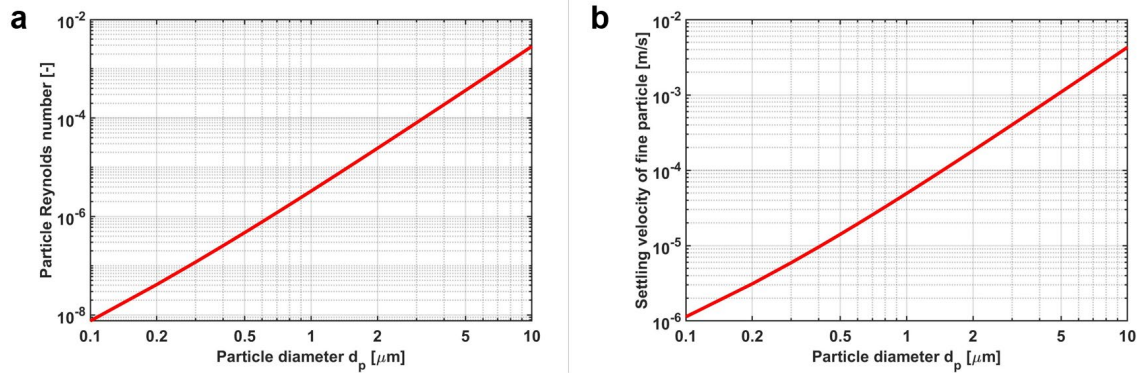
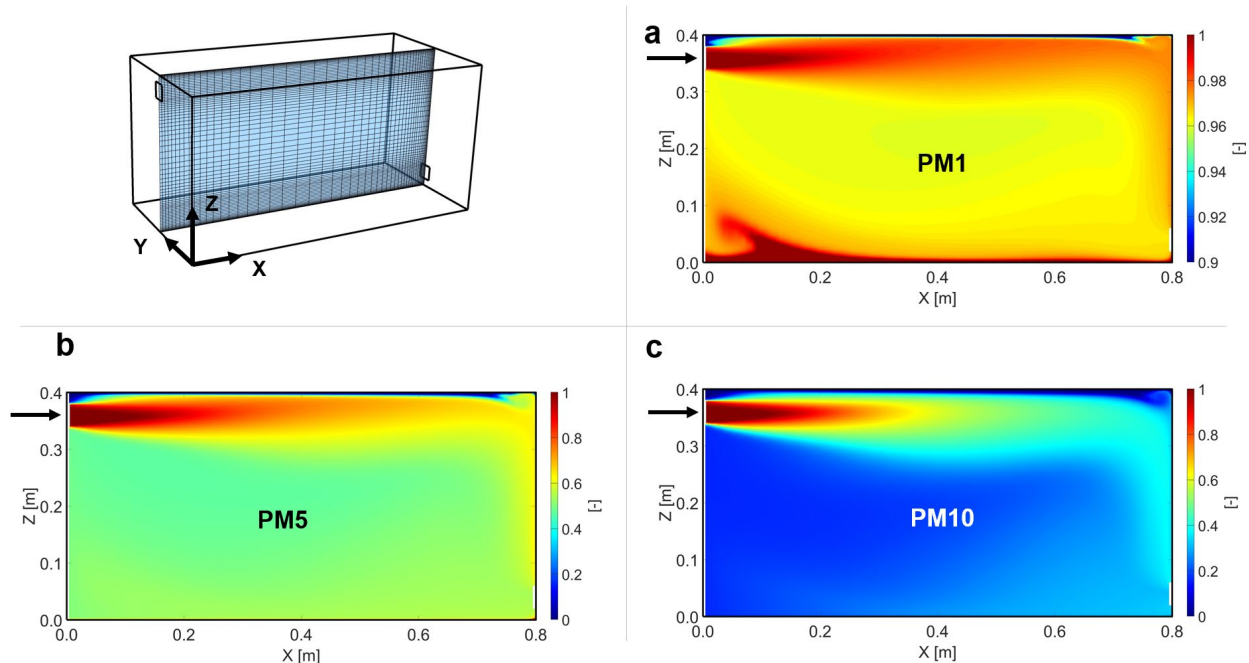**Figure 5.** Impact of particle size on the (a) particle Reynolds number and (b) particle settling velocity.

As shown in Table 1, the particle settling velocities are much smaller than 1 m/s when the particle diameter is equal to or smaller than 10 μm. For particles with a particle diameter smaller than 5 μm, the particle settling velocity is smaller than that of PM10 with more than one order of magnitude, indicating that the gravitational settling effects are minimal.

Table 1. Impact of particle size on the particle Reynolds number and particle settling velocity.

Particle diameter (μm)	Particle Reynolds number (-)	Particle settling velocity (m/s)
0.5	4.70×10^{-7}	1.41×10^{-5}
1	3.28×10^{-6}	4.93×10^{-5}
2	2.44×10^{-5}	1.83×10^{-4}
5	3.63×10^{-4}	1.09×10^{-3}
10	2.90×10^{-2}	4.29×10^{-3}

3.4.2. Particle concentration

Figure 6 shows the particle concentration (steady-state conditions) in the vertical central plane for different particle sizes. Note that the concentration ranges are different for different particle sizes to illustrate the concentration gradient. For particles with smaller sizes, the gravitational settling effects become less significant, resulting in more uniform distributions of particle concentration in the chamber, as shown in Figure 6. The uniform trend is consistent with the findings from other studies, such as Lai and Chen (2007) and Gao and Niu (2007). Lai and Chen (2007) reported that submicron particle concentration could achieve fairly uniform conditions in just 300 s in one empty ventilation chamber.

Note: the concentration ranges are different for different particle sizes to illustrate the concentration gradient.

Figure 6. Impact of particle size on the dimensionless particle concentration in the middle plane. (a) $d_p = 1$ μm. (b) $d_p = 5$ μm. (c) $d_p = 10$ μm.

Figure 7 compares the dimensionless concentration along three vertical lines in the vertical central plane. With the decreasing particle size, the dimensionless particle concentrations are closer to 1. The concentration gradient becomes much less for particle sizes smaller than 5 μm. In other words, the concentration in the room space tends to reach the concentration level at the inlet for very small particles ($d_p < 5$ μm). Several previous studies also reported that the drift term for particles less than 5 μm is negligible (Murakami et al., 1992; Holmberg and Chen, 2003; Zhao et al., 2004b; Zhang and Chen, 2007). Whereas Gao and Niu (2007) suggested a smaller top limitation to the particle size (2.5 μm), in which the gravitational settling effect can be ignored.
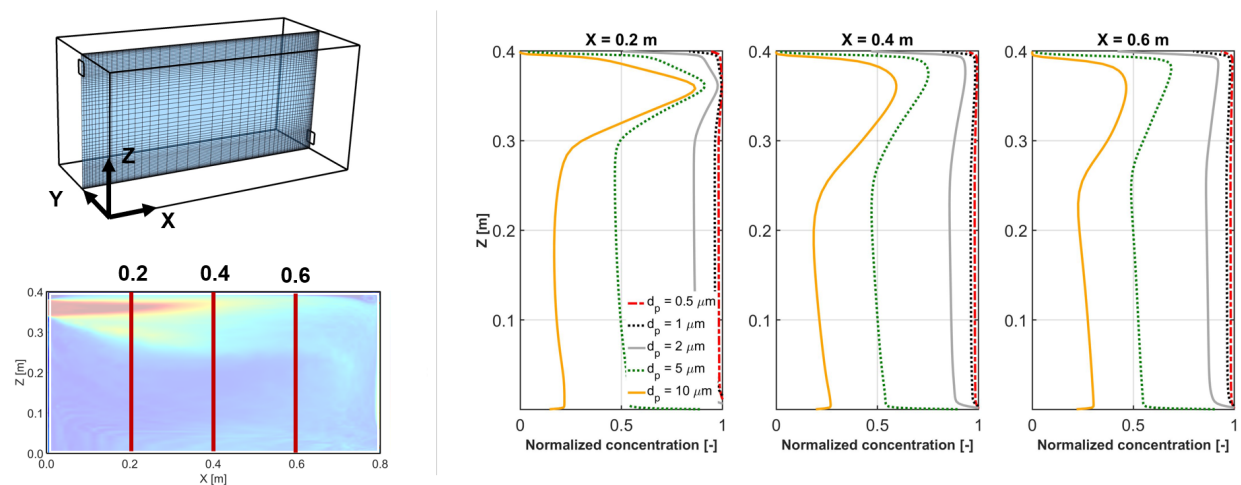
Figure 7. Impact of particle size on the dimensionless particle concentration along three vertical lines in the middle plane.

4. Modeling of respiratory emission

Olmedo et al. (2012) conducted a series of experiments on the distribution of exhaled contaminants and personal exposure in a room using tracer gas. Their measurement results are used here to validate the modeling approach of human respiratory emissions. Then, to find an efficient way to model particle emission of human breath, three different breathing modes are numerically examined:

1) Transient breathing model: sinusoidal function (sinusoidal).
2) Constant exhalation for source manikin and constant inhalation for target manikin (Ex & In).
3) Constant exhalation both for source manikin and the target manikin (Ex & Ex).

The comparisons in Section 3 demonstrate that the drift-flux model can predict particle dispersion in the indoor environment. Therefore, all simulations in this section were performed using the Eulerian drift-flux model.

4.1. Computational geometry and grid

Olmedo et al. (2012) conducted a series of experiments on the distribution of exhaled contaminants and personal exposure in a room using tracer gas. The configuration from their experiment is used to perform multiple steady and unsteady simulations of different breathing modes, as shown in Figure 8. The test room has dimensions of 4.10×2.68×3.19 m³ (L×H×W). Two thermal-breathing manikins stand face-to-face in the middle of the test room. The distance between them is 1.1 m. The manikin geometry was simplified using cubic boxes.
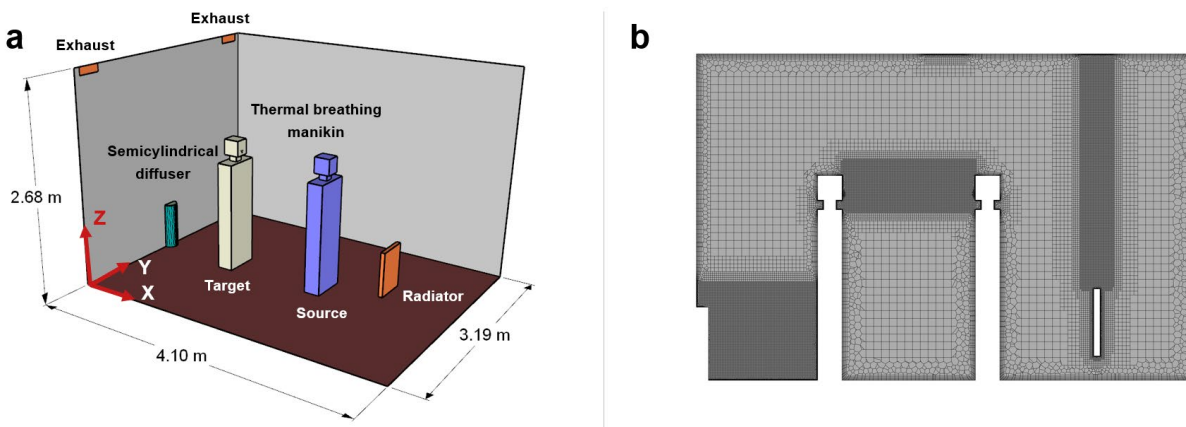

Figure 8. Simulation case of particle dispersion and deposition from human respiratory emissions. (a) Computational geometry for two thermal breathing manikins in a room space with displacement

ventilation. Replotted based on the experiment from Olmedo et al. (2012).
(b) Computational grid in the middle plane of the room width.

4.2. Boundary conditions

As from the experiment (Olmedo et al., 2012), a uniform velocity of 0.29 m/s was used for the semi-circular diffuser, normal to the curved surface, corresponding to 5.6 air changes per hour (ACH). The inlet air temperature was 16 °C. A pressure outlet was applied to the exhausts. The heat source for the radiator was 300 W, and the heat source was 94 W for each manikin, both of which were imposed using a surface heat flux (W/m^2), as shown in Table 2. For the wall surfaces of the room, an adiabatic boundary condition was imposed. All the surfaces had an emissivity of 0.9. Table 2 summarizes the boundary conditions used for the simulations in this section.

Table 2. Boundary conditions used for the simulation of two thermal breathing manikins.

Parameter	Area	Value	Heat source/ Temperature	Mass flux/ Mass fraction
Manikin surface	2.18 m^2	-	94 W (43.2 W/m^2)	-
Radiator	0.92 m^2	-	300 W (326.1 W/m^2)	-
Supply opening (displacement diffuser)	0.19 m^2	0.29 m/s (5.6 ACH)	16 °C	-
Mouth (source)	123 mm^2	See Table 3	34 °C	10^{-3}/0.027
Nose (target)	226 mm^2	See Table 3	34 °C	0
Ceiling, floor and side walls	-	Non-slip	Adiabatic wall	0 deposition flux on the floor

A sinusoidal function for the temporal velocity profile was used for the transient breathing mode (Villafruela et al., 2016). The maximum mouth velocities were 4.84 and 4.21 m/s for the source manikin and the target manikin, respectively. The frequency of breathing was 20 breaths/min for the source manikin and 15 for the target manikin.

$$V_{mouth} = \begin{cases} 4.84\sin\dfrac{2\pi}{3}t & \text{source, if } v > 0 \\ 4.21\sin\dfrac{\pi}{2}t & \text{target, if } v > 0 \end{cases}$$
(8)

Title
Progress report

Version
1.0

Page
14 of 41

$$V_{nostril} = \begin{cases} 2.636\sin\dfrac{2\pi}{3}t & \text{source, if } v < 0 \\[2mm] 2.293\sin\dfrac{\pi}{2}t & \text{target, if } v < 0 \end{cases} \tag{9}$$

The velocities for the steady breathing modes were determined based on the pulmonary ventilation rate of the source manikin (11.34 L/min) and the target manikin (9.90 L/min). Table 3 summarizes the velocity boundary conditions used for different breathing modes. In all simulations, the temperature of the exhaled air was 34 °C.

Table 3. Velocity boundary conditions for different breathing modes.

Manikin	1	2	3
Source	Sinusoidal cycle	Ex: 1.54 m/s (mouth)	Ex: 1.54 m/s (mouth)
Target	Sinusoidal cycle	In: -0.73 m/s (nose)	Ex: 1.46 m/s (mouth)

4.3. Solver settings

Steady Reynolds-averaged Navier-Stokes (RANS) simulations were performed using the RNG k-ε turbulence model (Yakhot et al., 1992) with low-Reynolds number modeling to solve the flow until the viscous sublayer (mean dimensionless wall distance ($y*$) is lower than 5). The surface-to-surface (S2S) radiation model was applied to model the radiative heat transfer. Second-order upwind discretization schemes were used for all variables. For pressure interpolation, a staggered scheme PRESTO! was applied. Pressure-velocity coupling was solved using the SIMPLE algorithm. The incompressible ideal gas law was used for buoyancy. The bounded second-order implicit scheme was applied for transient formulation.

A time step of 0.01 s was selected to simulate transient breathing mode. The first 1800 s (30 min) of the transient simulation were discarded to stabilize the room airflow. Then the statistical sampling was conducted for 360 s (10 min). For the steady breathing cases, based on sensitivity analysis, we found that the influence of the time step and the maximum iteration step per time step on the time-averaged results of the steady cases is minimal. Therefore, a large time step (5 s) with a small maximum iteration step (5) is used. Due to oscillatory behavior, the variables are averaged over 4000 time steps (20,000 s) to obtain a statistically steady solution in the steady breathing cases.

4.4. Validation study

Figure 9 compares the dimensionless air temperature ($(T-T_{in})/(T_{out}-T_{in})$) and the dimensionless pollutant concentration (c/c_R) obtained with CFD simulation (sinusoidal breathing cycle) and with experiment along three vertical lines, with T_{in} the inlet air temperature, T_{out} the average temperature at the exhaust and c_R the particle concentration at the exhaust. No experimental data on air temperature was reported for the two left lines, and for the middle line, no experimental data was reported on the dimensionless concentration. As can

be seen in Figure 9a, in general, the CFD simulation reproduces thermal stratification as from the experiment. The predicted dimensionless air temperatures are slightly smaller than the experimental results.

Compared to the experiment, the CFD simulation also reproduced the concentration stratification (Figure 9b). Below the mouth height, the concentration is nearly zero, and on top of the target manikin, the concentration reaches its highest. However, along the line of X = 3.70 m, the high concentration at the normalized height of 0.46 was not reproduced from the CFD simulation. This can be attributed to the geometrical simplification of the thermal manikins. In the simulation, the detailed nose geometry was not included. In the experiment, it was reported that the nose surface faced downwards at a direction of 45° below the horizontal plane.
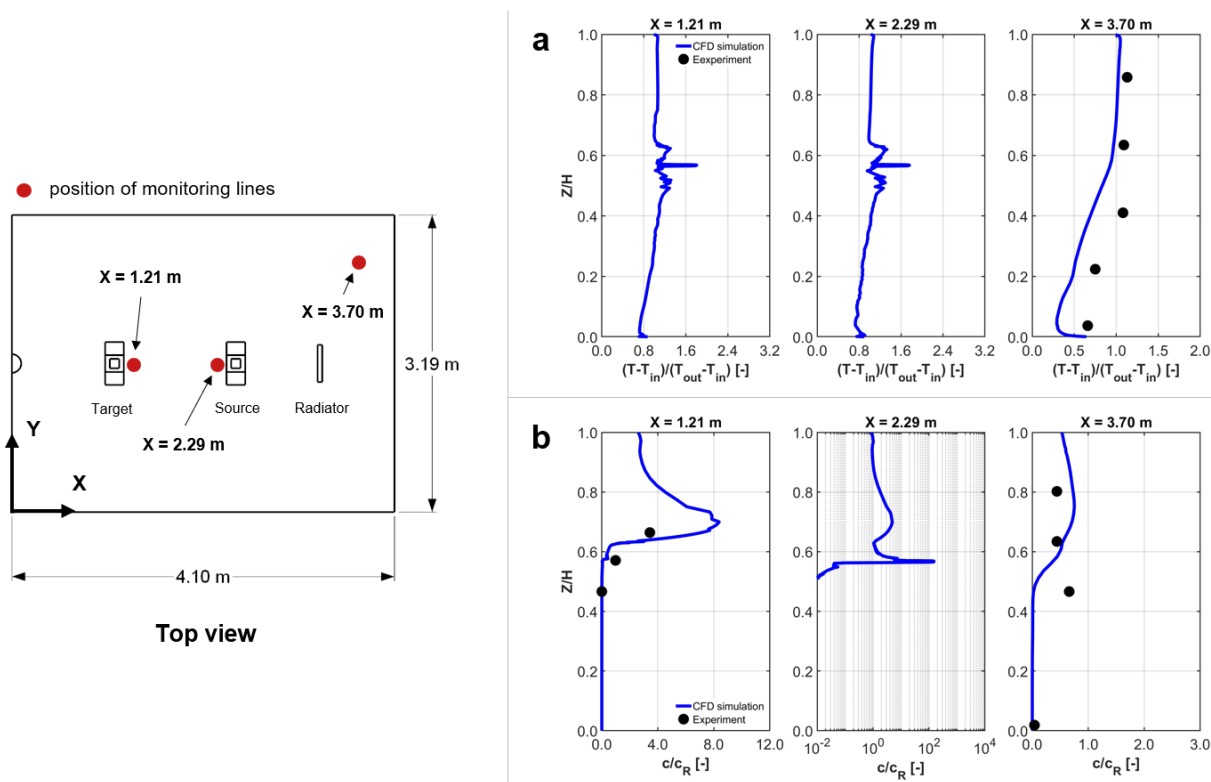

Figure 9. Comparison of dimensionless air temperature and dimensionless pollutant concentration obtained with CFD simulation of the sinusoidal breathing cycle and with experiment. In the experiment, the air temperature was only measured along the vertical line of X = 3.70 m, and concentration was measured along two vertical lines (X = 1.21 m and X = 3.70 m).

From the animations (not shown here), we found that in this configuration, where the distance between the two manikins is 1.1 m, there is an interaction between the two mouth jets. Figure 10 shows the time-averaged air distributions in the vertical central plane of the investigated room. Due to a higher maximum velocity, the mouth jet of the source manikin is stronger than that of the target manikin. The thermal effects of human beings and radiator on air movement are significant (Figure 10a-b). The thermal plumes from the two manikins induce two upward air flows around them, with air speeds of around 0.15 m/s. The particle dispersion between the two thermal manikins is thus restricted by the

thermal plumes. From Figure 10c and Figure 10d, a high concentration exists between the two manikins. Below the half height of the test room, due to the application of displacement ventilation, the particle concentration is near 0 in this configuration. In addition, from the distributions of dimensionless concentration on tracer gas (Figure 10c) and PM1 (d_p = 1 μm) (Figure 10d), the difference between them is slight, implying that tracer gas can reproduce the particle dispersion with submicrometric sizes. Therefore, it is suitable to utilize a passive scalar to model the airborne transmission of very fine particles. To learn more about the impact of particle size on the particle dispersion in a room space, a sensitivity analysis of particle size is discussed in Section 4.5.2.
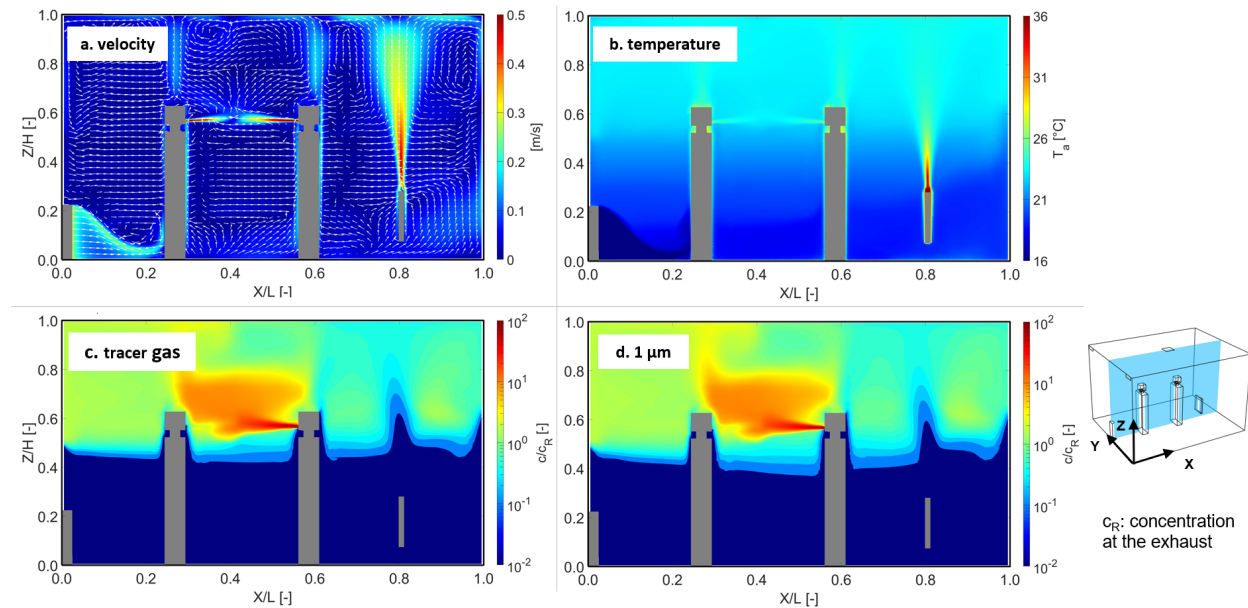

Figure 10. Air distributions in the vertical central plane. (a) Velocity magnitude and velocity vectors. (b) Air temperature. (c) Dimensionless concentration of tracer gas. (d) Dimensionless particle concentration of PM1 (d_p = 1 μm)

4.5. Results and discussion

In total three cases, i.e., one transient case and two steady cases, are modeled to investigate the effect of the human respiratory emission of virus-laden particles (Table 3). As mentioned before, the three different breathing modes are:

1)   Transient breathing model: sinusoidal function (sinusoidal).
2)   Constant exhalation for source manikin and constant inhalation for target manikin (Ex & In).
3)   Constant exhalation both for source manikin and the target manikin (Ex & Ex).

4.5.1. Air velocity and air temperature

Figure 11 compares the distribution of velocity magnitude and velocity vector in the vertical central plane from different human breathing modes. A clear difference can be observed in the region between the

two breathing manikins at the mouth height. For case 2, i.e., constant exhalation for source manikin and constant inhalation for target manikin, the velocities near the mouth and nose of the target manikin are relatively small compared to the other two cases. Moreover, the buoyancy effects are stronger under the steady state than in the transient breathing mode. Due to a higher air temperature of the exhaled air, the mouth jets travel a little bit upwards in cases b and c.

On the other hand, the influence of the breathing mode on the general flow pattern in the room is negligible, which is also supported by other studies (Villafruela et al., 2013b, 2016). As shown in Figure 12, the distributions of air temperature follow the flow patterns of air velocity. Thermal plumes are observed for the thermal manikins and the radiator.
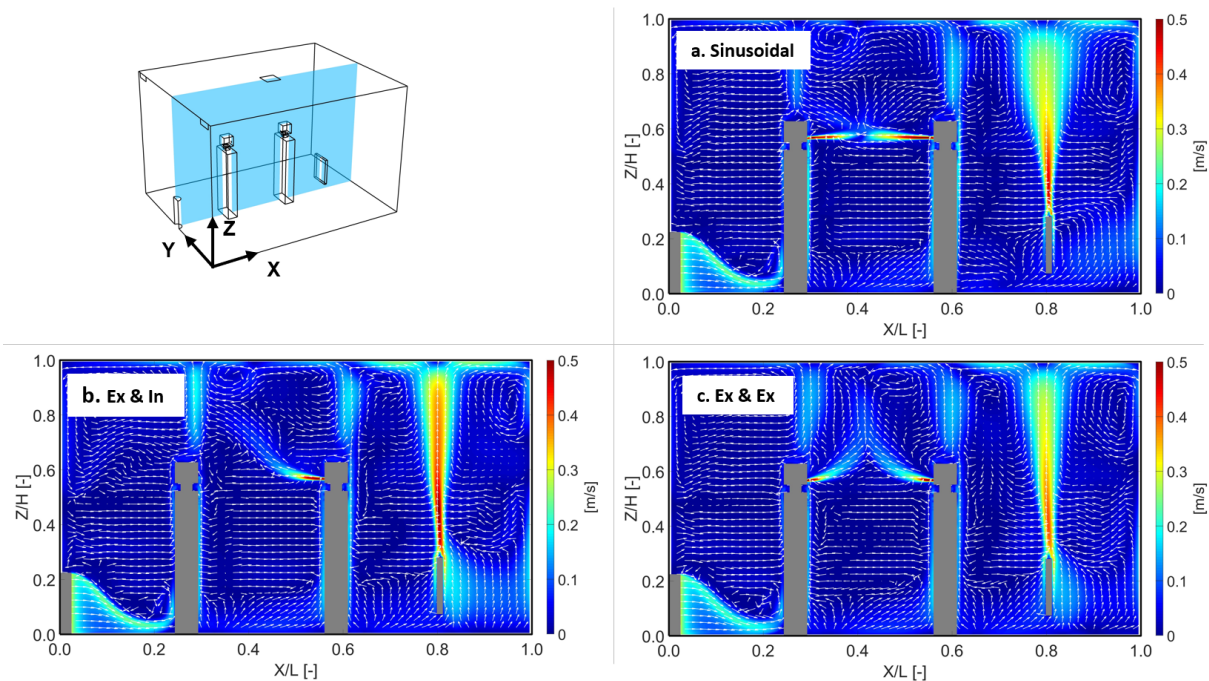

Figure 11. Distribution of velocity magnitude and velocity vector in the vertical central plane. (a) Sinusoidal breathing cycle. (b) Constant exhalation for source manikin and constant inhalation for target manikin. (c) Constant exhalations both for source manikin and target manikin.
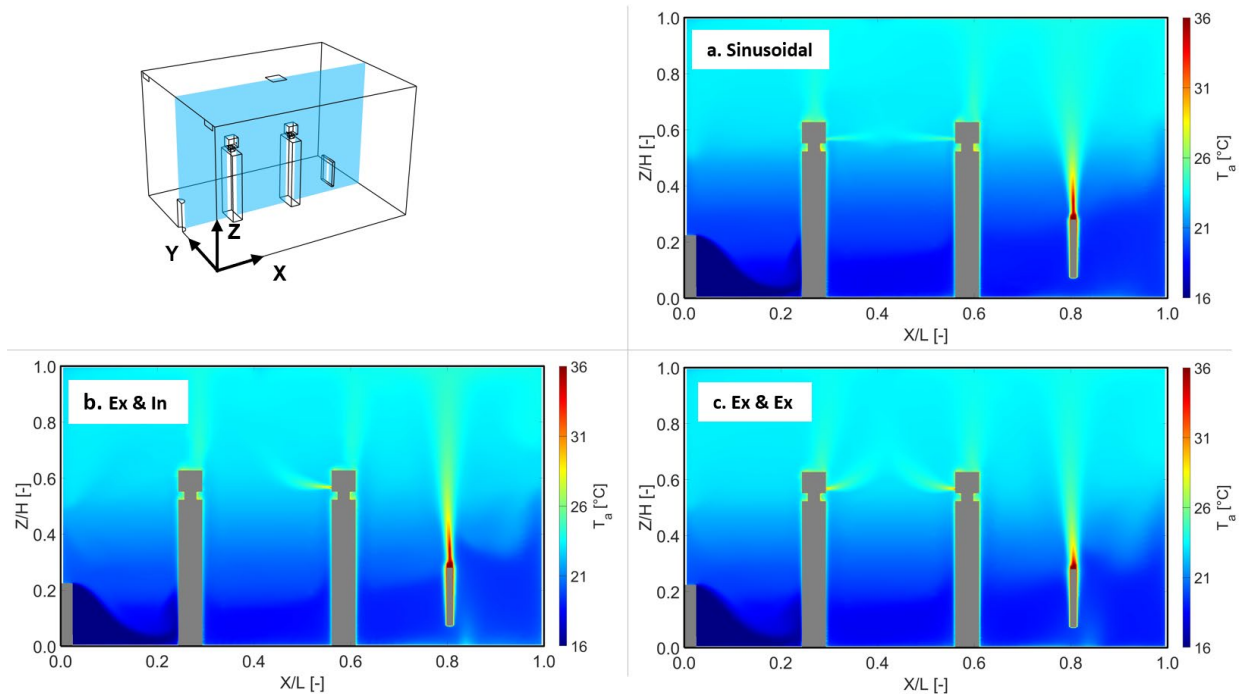
Figure 12. Distribution of air temperature in the vertical central plane. (a) Sinusoidal breathing cycle. (b) Constant exhalation for source manikin and constant inhalation for target manikin. (c) Constant exhalations both for source manikin and target manikin.

4.5.2. Impact of particle size

As mentioned above, clear concentration stratification can be found in the particle dispersion in a room space with displacement ventilation for tracer gas and PM1 (Figure 10). Figure 13 compares the dimensionless particle concentration obtained from different particle sizes. The particle settling velocities of PM5 and PM10 are in the order of magnitude of 10^{-3} (Table 1), and their settling effects are significant in the particle dispersion and deposition. The dimensionless concentrations in the lower part of the room are much larger than those for small particles (PM1 and PM2). On the other hand, the distributions are quite similar between PM1 and PM2. Based on the simulation results in Section 4.4 (Figure 10) and Figure 13, it can be concluded that a passive scalar without gravitational effect is suitable in the modeling of particle dispersion for very fine particles ($d_p \leq 2$ μm). The top limitation to the particle size reported in other studies is 2.5 μm (Gao and Niu, 2007) or 5 μm (Murakami et al., 1992; Holmberg and Chen, 2003; Zhao et al., 2004b; Zhang and Chen, 2007).
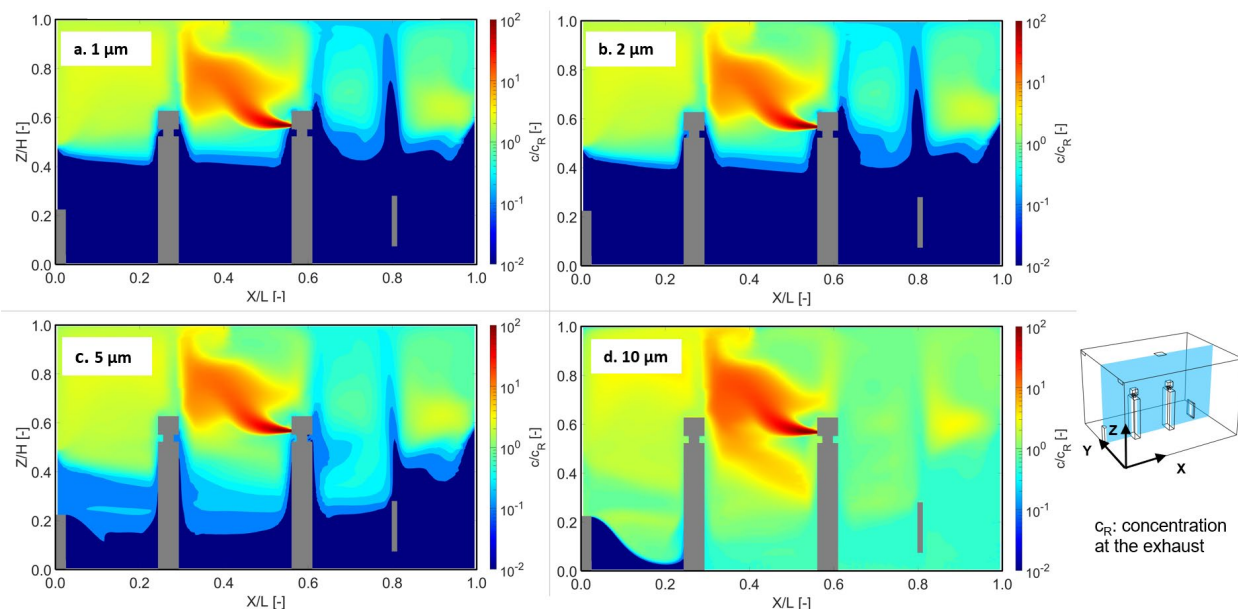
Figure 13. Comparison of dimensionless particle concentration in the middle plane of Y axis obtained from different particle sizes. Note that constant exhalation and inhalation rates are used for the source and target manikin, respectively. (a) d_p = 1 μm. (b) d_p = 2 μm. (c) d_p = 5 μm. (d) d_p = 10 μm.

4.5.3. Impact of breathing mode

The simulation results of tracer gas (TG), PM0.5, PM1, and PM 2 are very close to each other. Herein, only the distributions of PM1 (d_p = 1 μm) from different breathing modes are demonstrated. Figure 14 compares the concentration distribution of PM1 in the vertical central plane of the tested room. The concentration is normalized by the average concentration at the exhausts (c_R). Note that a logarithmic scale is used for the colormap to illustrate the concentration gradient clearly.

The distributions between case 1 (transient breathing mode) and case 2 (steady exhalation & inhalation) are nearly similar. In most regions, the dimensionless concentration is in the same order of magnitude, indicating that the steady velocity boundary conditions can reproduce the main features of particle dispersion from human breath to a large extent. However, a slight difference can be found between case 1 and case 2. Compared to the transient breathing mode (case 1), in case 2, the particle cloud between the two manikins reaches a higher position above the target manikin. In contrast, the particle concentration distribution in case 3 (steady exhalation & exhalation) deviates significantly from the transient breathing mode. Exhaled flow through an infected individual's mouth can easily penetrate a nearby individual's breathing region, while exhaled flow through the mouth of an exposed individual has a cleaning effect on the breathing region (Ai and Melikov, 2018). As a result, a steady exhalation boundary at the mouth for the target manikin prohibits particle dispersion from the source manikins, as shown in Figure 14c. The particle concentration near the mouth and nose of the target manikin is much smaller than in the other two cases (case 1 and case 2, Figure 14a-b). Moreover, in case 3, the particle concentration behind the source manikin is smaller than in the other two cases. Three performance indicators are compared in the next sub-section to assess the different modeling methods quantitatively.
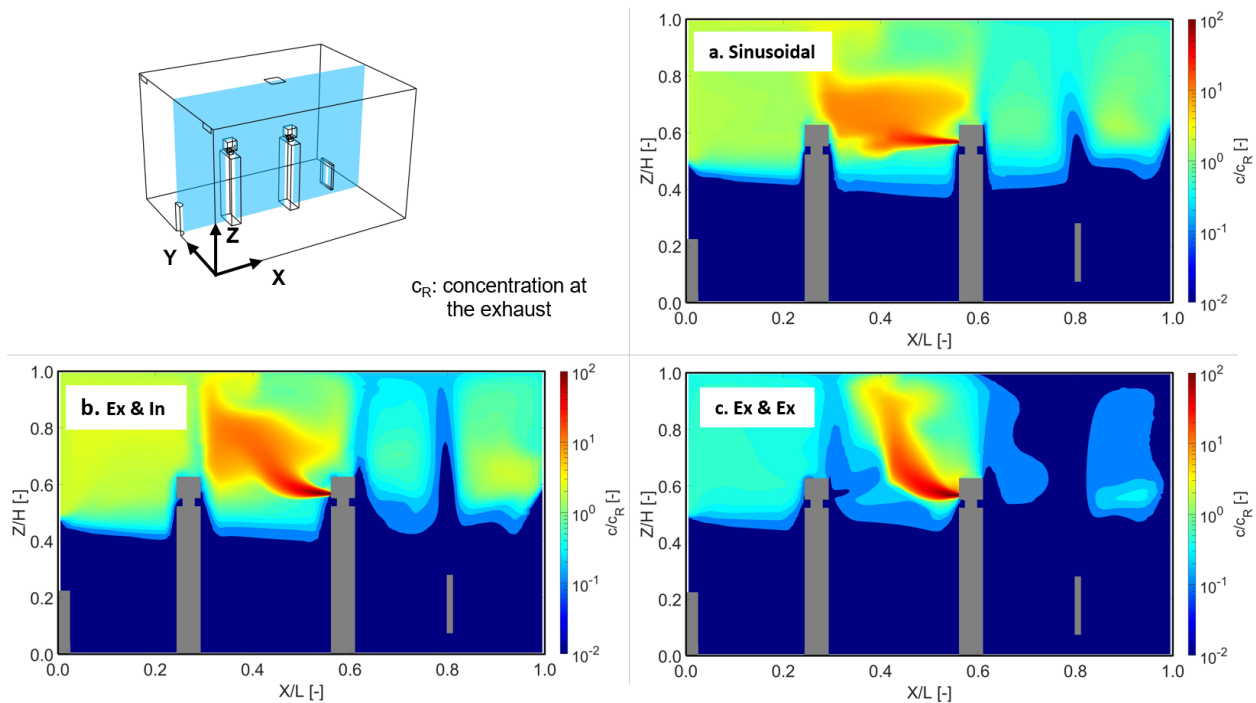
Figure 14. Distribution of dimensionless concentration of PM1 ($d_p = 1$ μm) in the middle plane of Y axis. (a) Time-averaged results from sinusoidal breathing cycle. (b) Constant breathing rate: exhalation for source manikin and inhalation for target manikin. (c) Constant breathing rate: exhalation for source manikin and exhalation for target manikin.

4.5.4. Performance indicators

To quantify the ventilation performance in pollutant removal and the cross-infection risk, the intake fraction (Section 2.4.1), the exposure index at the nose surface, and the exposure index at the breathing zone are calculated and compared for different breathing modes, as shown in Figure 15. The exposure index is defined as the proportion of average concentration at the nose surface (or the breathing zone) and the average concentration at the ventilation exhausts. A cubic volume of $10 \times 10 \times 10$ cm^3 near the mouth and nose of the target manikin is used for the breathing zone in the present study.

Since there is no inhalation in case 3 for the target manikin, the intake fraction is zero (Figure 15a). Compared to the case of the sinusoidal breathing cycle (case 1), the intake fractions are much smaller in case 2 due to a lower concentration near the nose. On the other hand, the intake fractions increase with the increase of the particle size.

The exposure indexes are in the same order of magnitude for different particle sizes. However, large differences can be found in different breathing modes. This is attributed to the fact that the velocity boundary conditions of breathing highly influence the micro-environment near the mouth and nose of the target manikin. The maximum mouth velocity is above 4 m/s in the transient breathing case. In contrast, the mouth velocity is 1.54 m/s for the steady breathing modes, which is less than half of the maximum velocity from the transient breathing case. Therefore, the expiratory particles from the source manikin cannot travel that far to the target manikin in the steady breathing case. However, from Figure 14, the distributions of normalized concentration in most regions are relatively similar between case 1 (transient) and case 2 (constant exhalation for both manikins) in a logarithmic scale.
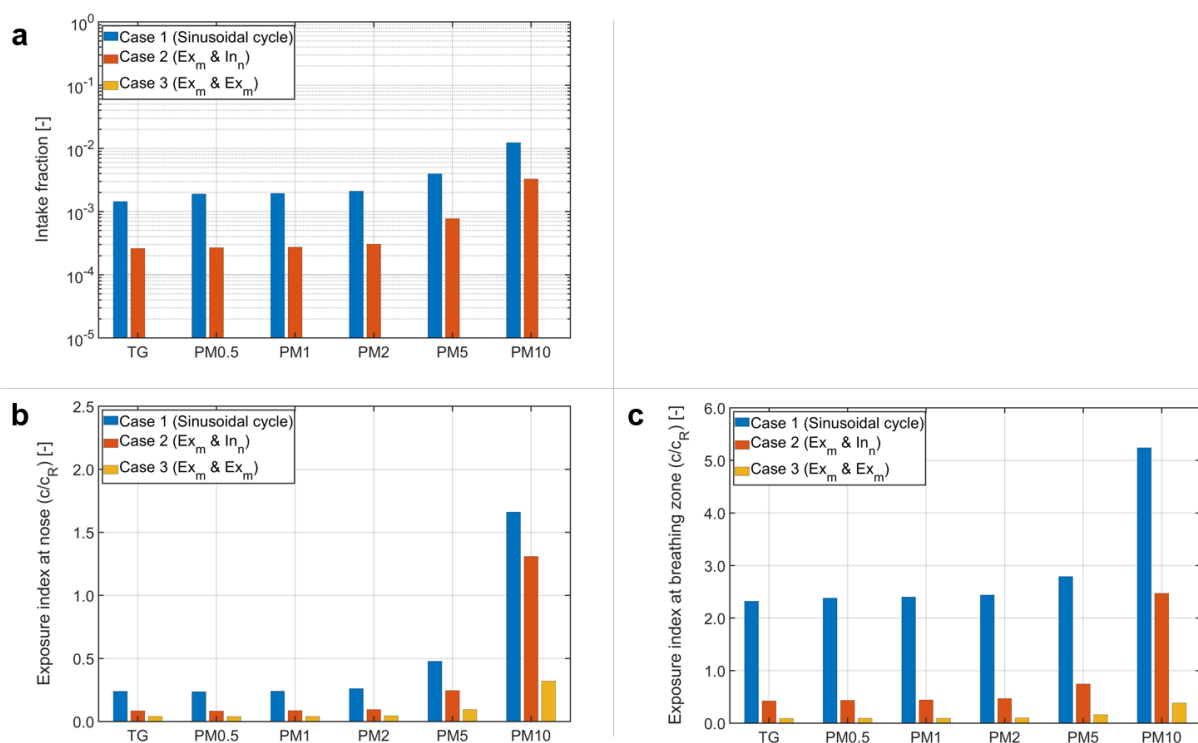
Title
Progress report

Version
1.0

Page
21 of 41

Figure 15. Comparison of performance indicators from different breathing modes for different particle sizes. (a) Intake fraction. (b) Exposure index at the nose surface. (c) Exposure index at the breathing zone.

Many studies report uncertainties on many influencing factors for the modeling and measurement of expiratory particles in indoor environments (e.g., Ai and Melikov, 2018; Nazaroff, 2022). Therefore, for the design of ventilation systems, the simulation of steady breathing mode appears to provide reasonable accuracy with respect to the prediction of particle dispersion. However, care should be taken on the selection of mouth velocity for the source manikin when using steady breathing mode for simulation. An average velocity based on the pulmonary ventilation rate underestimates the particle dispersion in the horizontal direction.

5. Modeling of human movement

A transient simulation with dynamic mesh is the most frequently used method to model human movement in the simulation of indoor airflow, which takes considerable computational resources. To find a simple method to model human movement, the following four modeling methods are tested and compared in the same room space of Section 4:

(a) Explicitly modeled moving person using overset mesh.
(b) Momentum source in the moving zone without adding the heat source of the moving person.
(c) Momentum and heat sources from moving person in the moving zone.
(d) Without moving person.

5.1. Computational geometry and grid

Figure 16a shows the layout for the simulation of human movement. This section uses the same room space, ventilation and heating systems, and source manikin configurations as in Section 4. To model the human movement, the target manikin is placed in the left corner of the room, and the source manikin faces the moving direction of the target manikin. In the simulations, a moving speed of 0.2 m/s and a moving duration of 15 s is used. Therefore, the total moving distance is 3 m. To include all the geometries of the target manikin (moving person) during the movement, the moving zone is set as 3.5 m in length and 1.8 m in height.

Compared to the dynamic mesh method, where the mesh needs to be updated after each or several time steps, overset mesh is a fast and efficient way to model a moving component in CFD simulation. Therefore, the overset mesh was applied to model human movement. Two grids need to be prepared when using overset mesh method, i.e., the background grid and the moving component grid. In the present study, the background grid was refined in the moving zone, i.e., the yellow-colored zone as shown in Figure 16a. A finer grid was used for the moving component grid (target person), as shown in Figure 16b. In the simulation, the component grid was set as a moving zone with an X-velocity of 0.2 m/s. Thus, the component grid oversets the background grid during the simulation, which is the reason why it is called the overset mesh method.
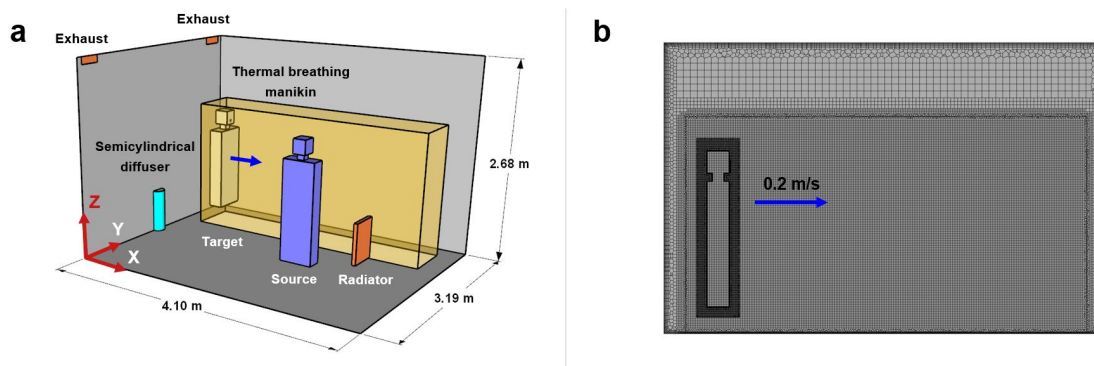

Figure 16. Simulation case of human movement: (a) computational geometry and (b) computational grid in the middle plane of target manikin along Y axis.

5.2. Boundary conditions and solver settings

The steady breathing mode used in Section 4 (Case 2) reproduces the particle dispersion to a certain extent. It was also used in this section to perform the CFD simulations of human movement. As shown in Table 3, the source manikin exhaled virus-laden particles at a constant rate with a velocity of 1.54 m/s at the mouth. The inhalation velocity for the target manikin was -0.73 m/s at the nose. Identical boundary conditions were applied to simulate moving manikin, as in Section 4. Table 2 summarizes the boundary conditions used in the simulations. In addition, the solver settings were identical to those in Section 4. For the sake of brevity, they are not introduced here again.

In the case of the explicitly modeled moving manikin, the flow field was initialized by a transient simulation when the moving manikin was at the starting position. A time step of 0.01 s was applied during the human movement, and a maximum number of iterations of 10 was applied for each time step. The radiation was not modeled due to the restriction in using overset mesh.

In case 2 and case 3, the momentum source was added in the moving zone based on the following equation (Brohus et al., 2006; Cao et al., 2017; Ren et al., 2019):

Title
Progress report

Version
1.0

Page
23 of 41

$$F = \frac{1}{2}\rho_a U_{moving}^2 A \qquad (10)$$

where ρ_a is the air density; U_{moving} is the moving velocity of the moving person; A is the frontal area of the moving person.

5.3. Simulation results with an explicitly modeled moving manikin

5.3.1. Vertical central plane of the moving zone

Figure 17 shows the time evolution of air velocity in the vertical central plane of the moving zone. At the starting point, the air speeds are lower than 0.1 m/s in the moving zone. During movement, significant horizontal airflow is generated around the moving manikin. A high air speed region gradually forms behind the moving manikin. The area of the increased air speed region becomes stable from the time t = 9 s. The air speeds in front of the moving manikin are much lower than those behind. In addition, the air velocity directions in the vicinity of the moving manikin are parallel to the moving direction.

Figure 18 shows the time evolution of air temperature. At the starting time, a vertically distributed thermal plume exists above the moving manikin. After the manikin starts to move, the thermal plume gradually becomes horizontally distributed. Meantime, a slightly higher temperature region can be found behind the moving manikin during the movement.

Figure 19 shows the time evolution of dimensionless particle concentration for PM1 (d_p = 1 μm), in which the particle concentration is normalized by the average exhaust concentration. At the starting time, in front of the source manikin, the particle concentration is high due to the exhaled particles from the source manikin. The moving person can disturb the high-concentration region when moving to the central part of the room. Then, within several seconds, the high concentration gradually recovers behind the moving person after the disturbance.
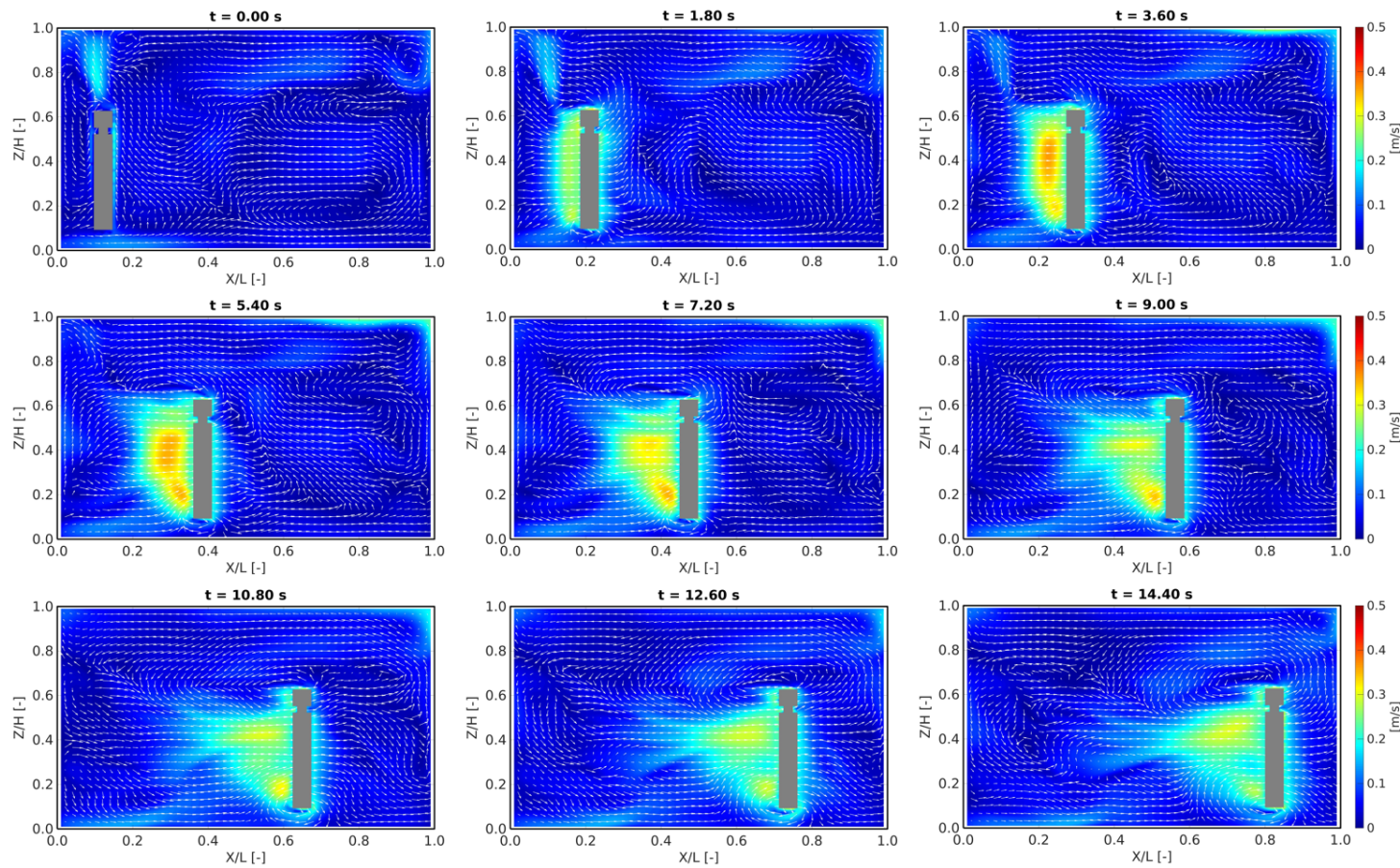
Figure 17. Time evolution of air velocity in the vertical central plane of the moving zone.
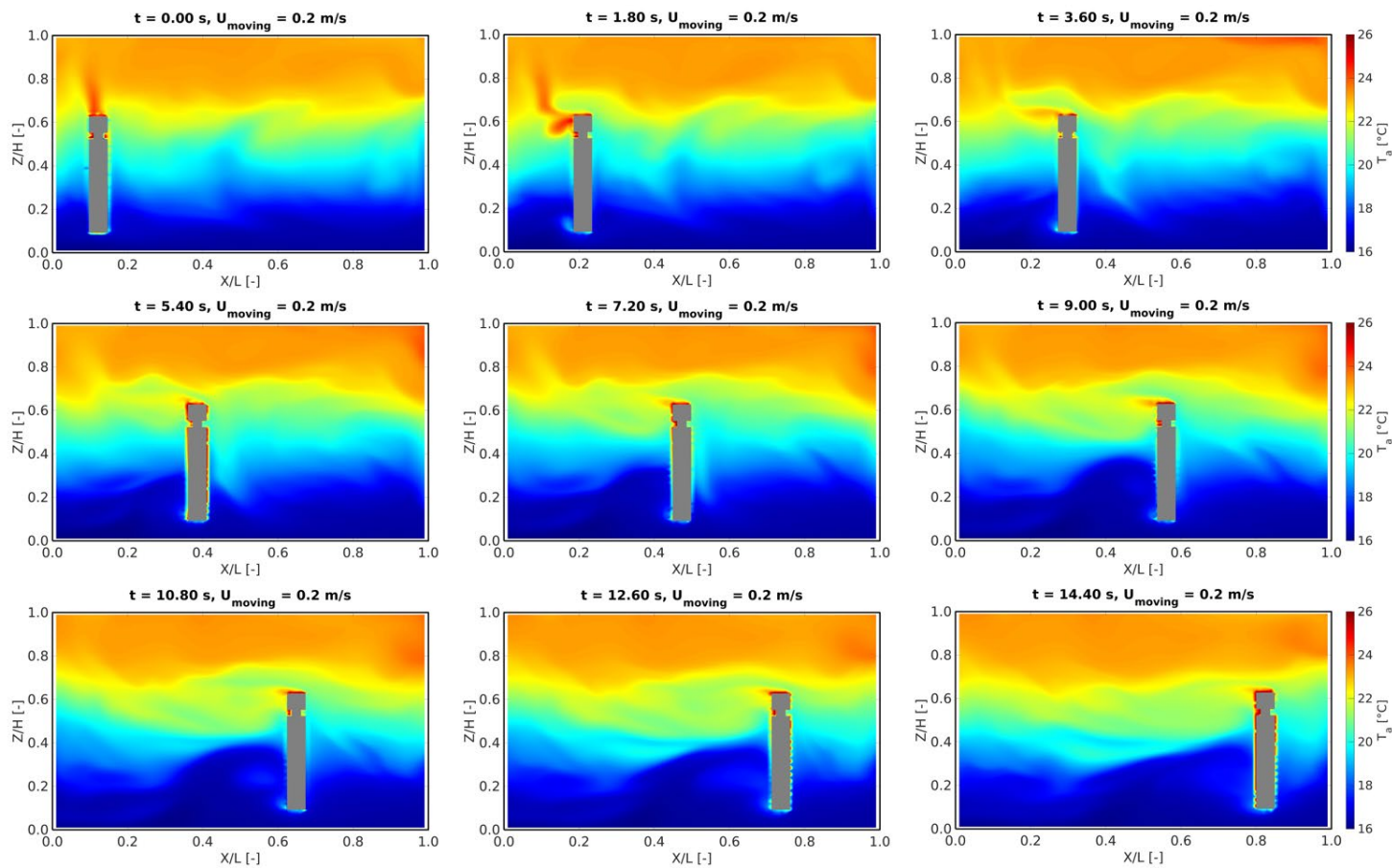
Title
Progress report

Version
1.0

Page
25 of 41

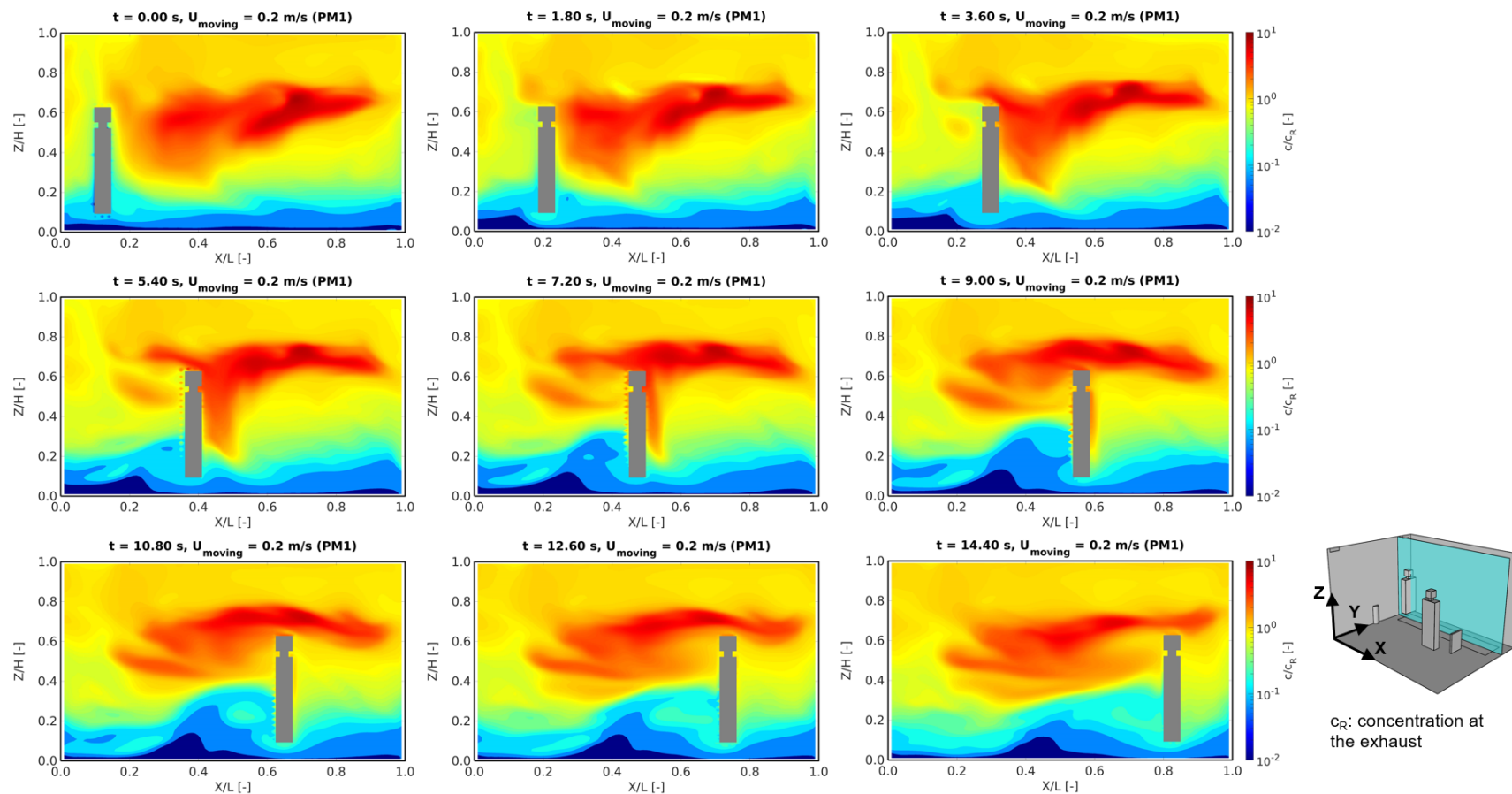**Figure 18.** Time evolution of air temperature in the vertical central plane of the moving zone.

Figure 19. Time evolution of dimensionless particle concentration in the vertical central plane of the moving zone for PM1 (d_p = 1 μm).

Title
Progress report

Version
1.0

Page
27 of 41

5.3.2. Horizontal plane at the mouth height

Figure 20 shows the distributions of velocity and vector at the mouth height. At the starting point, the airflow in this plane is dominated by a counter-clockwise recirculation. The human movement adds extra momentum to the room and thus resulting in higher air speeds in this plane. A clear wake region is observed behind the moving person, where the air speed is close to the moving speed (0.2 m/s). Moreover, the airflow direction in the moving zone changes to the moving direction, opposite to the initial direction at the starting time. However, in the lower part of this plane, although the velocity magnitude changes slightly during the movement, the airflow directions stay almost the same as the starting time.

The air temperature distribution (Figure 21) follows the velocity distribution pattern in the horizontal plane at mouth height. At the starting time, a ring region of slightly higher air temperature exists around the source manikin. Human movement changes the initial temperature pattern. On the left of the source manikin, the air temperature increases from t = 1.8 s to t = 9.0 s and then recovers to the initial air temperature at t = 15 s.

Due to the exhaled particles from the source manikin, a high-concentration region is observed in front of the source manikin at the mouth height (Figure 22). From the starting point, the moving manikin gradually enters this high-concentration region. In the wake region of the moving manikin, the particle concentration is slightly lower than the ambient from t = 0 to t = 7.2 s but is high near the mouth and nose of the moving manikin. From t = 9.0 s, the particle concentration in front of the moving person becomes much lower than before.
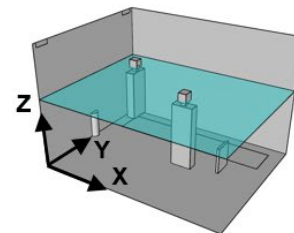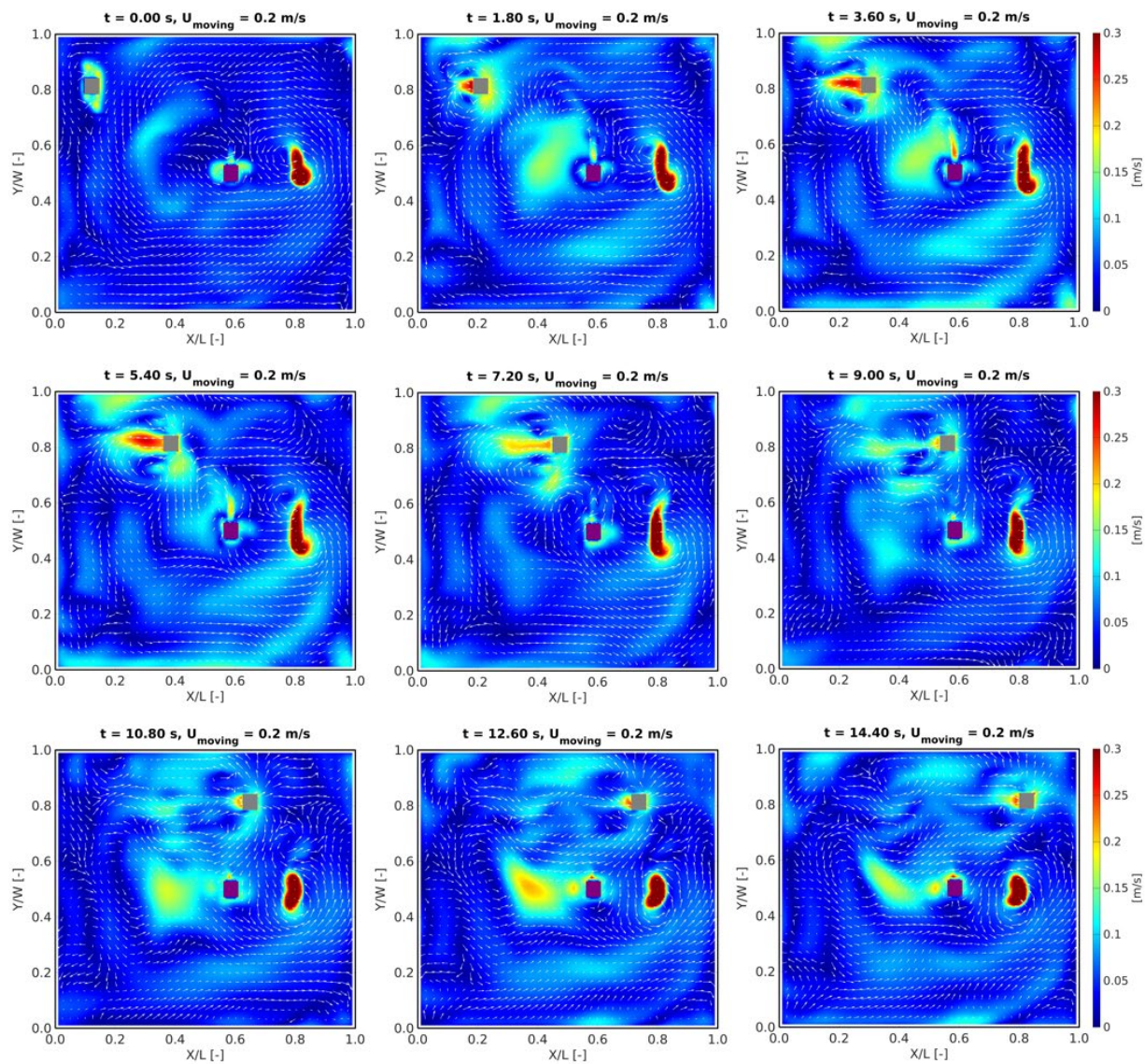
Figure 20. Time evolution of velocity magnitude and velocity vector in the horizontal plane of the mouth height.

Title
Progress report

Version
1.0

Page
29 of 41
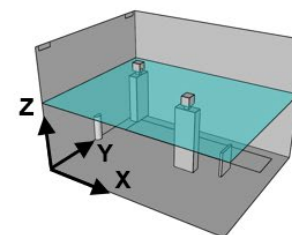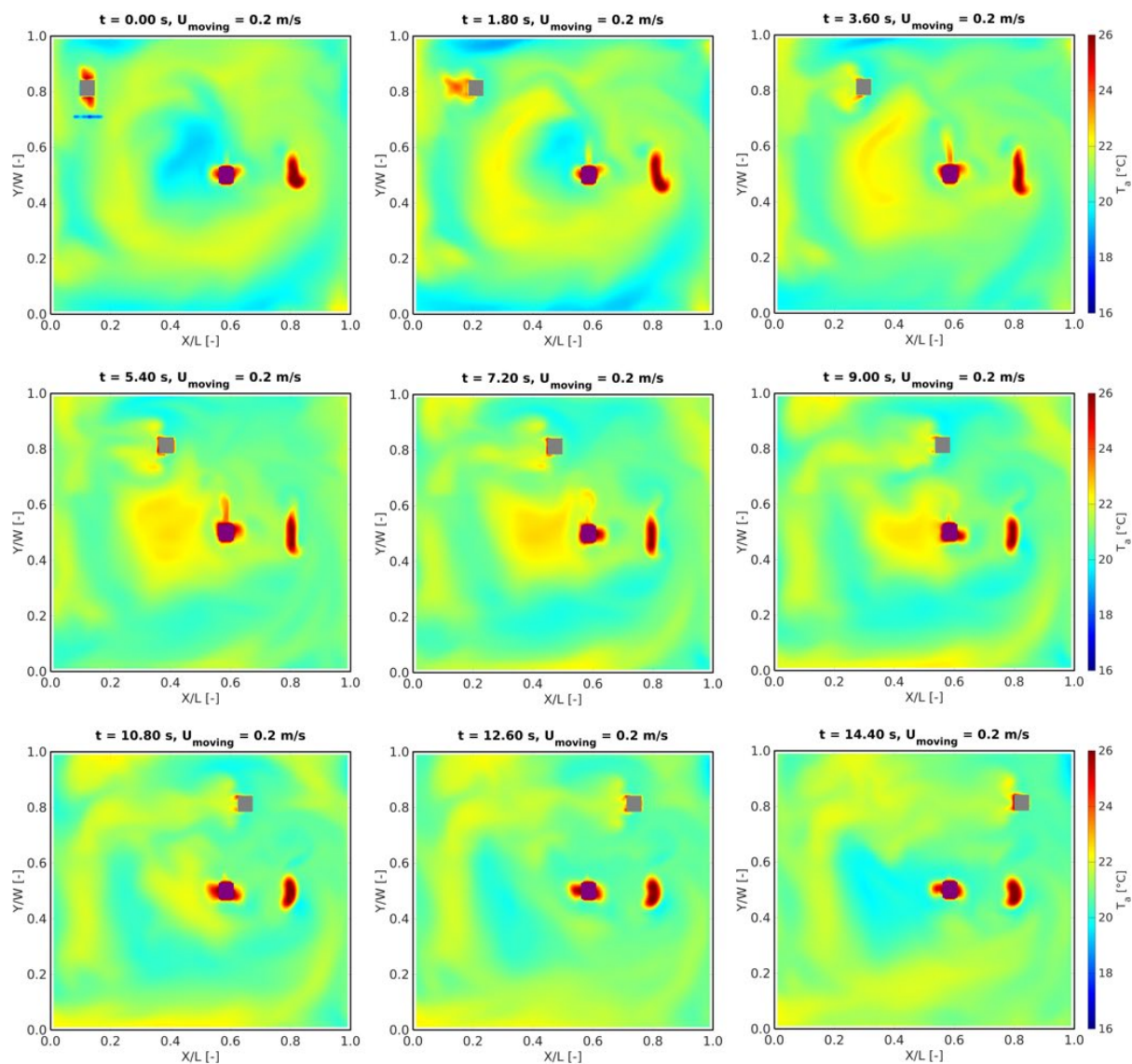
Figure 21. Time evolution of air temperature in the horizontal plane of the mouth height.

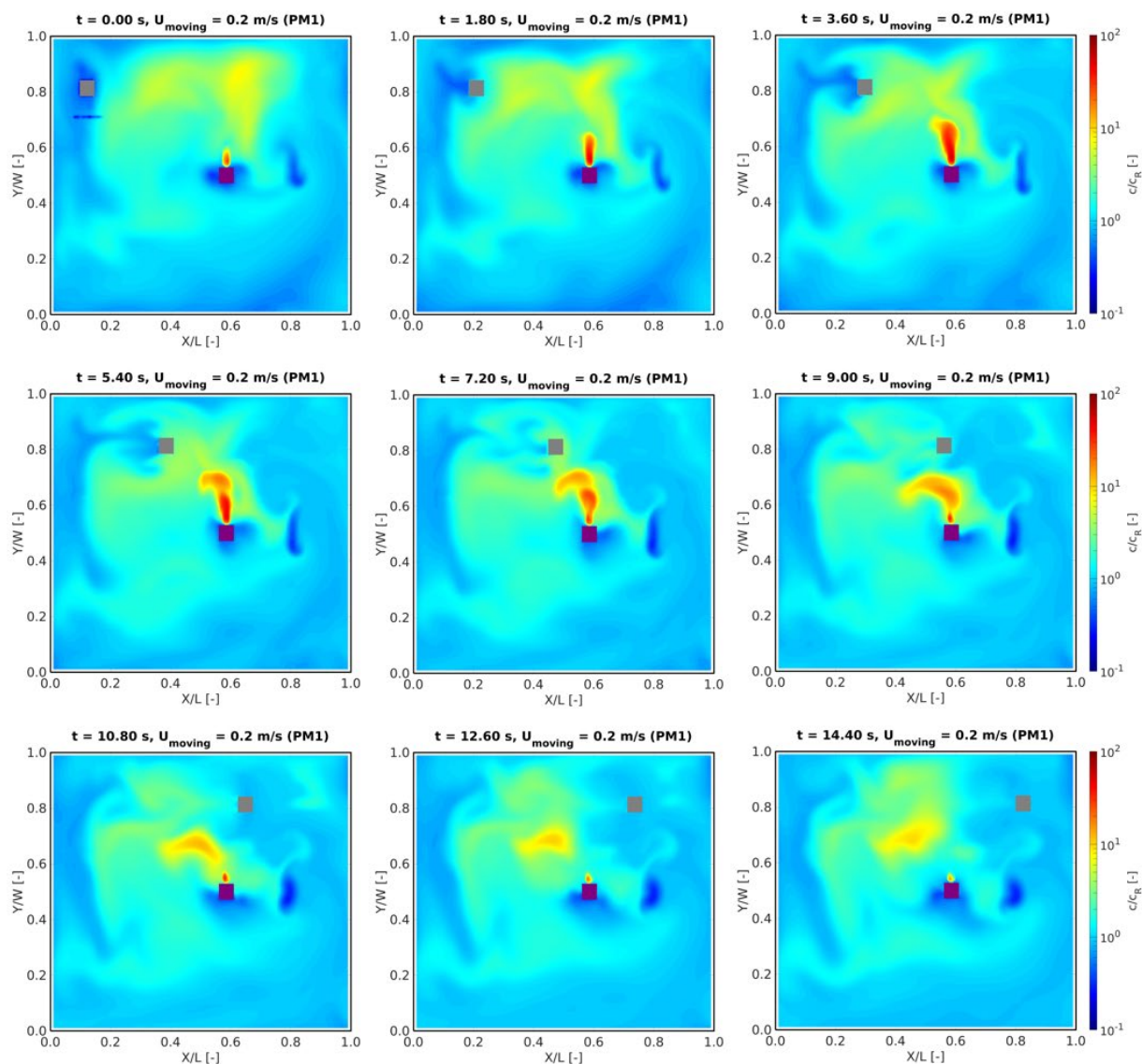| Title	Version	Page
2022 Report: IEA EBC annex-86 Energy Efficient IAQ Management	**1.0**	30 of 41
in residential buildings		

Figure 22. Time evolution of dimensionless particle concentration in the horizontal plane of the mouth height for PM1 ($d_p = 1$ μm).

Title
2022 Report: IEA EBC annex-86 Energy Efficient IAQ Management
in residential buildings

Version
1.0

Page
31 of 41

5.4. Comparison between explicitly modeled moving manikin and momentum source

In this sub-section, the simulation results of four different cases are compared. As mentioned above, the first case is the transient case with moving manikin using the overset mesh method, and the other three are steady-state results. For the first case, the results shown in this sub-section are averaged for the 15 s of the moving period.

5.4.1. Vertical plane along the target manikin

Figure 23 shows the distribution of air velocity in the vertical central plane of the moving zone for the four different modeling cases. Due to human movement, the air speed in the moving zone is relatively higher than the other regions in this plane, which are predicted in cases a, b and c through different methods. However, the air speeds from the momentum source method (cases b and c) are slightly larger than those from the explicit modeling method (case a). Moreover, the high-speed region in case a is on the left, whereas it is on the right in cases b and c. If the human movement is not modeled, the air speed in the moving zone is very low (case d). Similar velocity distributions are observed between case b and case c, indicating that the influence of the heat source on the simulation results of the momentum source method is limited.

Without adding the heat source from the moving manikin, the air temperature at the higher part can be two degrees lower than with the heat source (Figure 24). The temperature distribution obtained with momentum and heat sources (case c) is close to that of explicit human movement modeling (case a). The main difference lies in that there is a thin layer of high air temperature near the top boundary of the moving manikin in the explicitly modeled case (case a), which is induced by the increased air temperature above the head of the moving manikin from the thermal plume (Figure 18).

Figure 25 compares the dimensionless concentration of PM1 in the vertical central plane of the moving zone. In case a, it can be found that the human movement enhances the air mixing in the room, and thus the concentration distribution is more uniform compared to a still case, e.g., Figure 10c. However, the entrainment of particle dispersion near the floor cannot be reproduced well by adding a fixed source term in the moving zone (case b and case c in Figure 25). Due to a stable flow field in case b and case c, the concentration stratifications observed are stronger than case a. In addition, the dimensionless concentration at the breathing height (1.60 m, Z/H = 0.60) is slightly smaller in cases b and c (momentum source) compared to the explicit modeling method (case a). Interestingly, the difference in concentration distribution at the mouth height is minimal between case a (moving manikin) and case d (without moving manikin), which means the influence of human movement on particle dispersion is limited in this configuration.
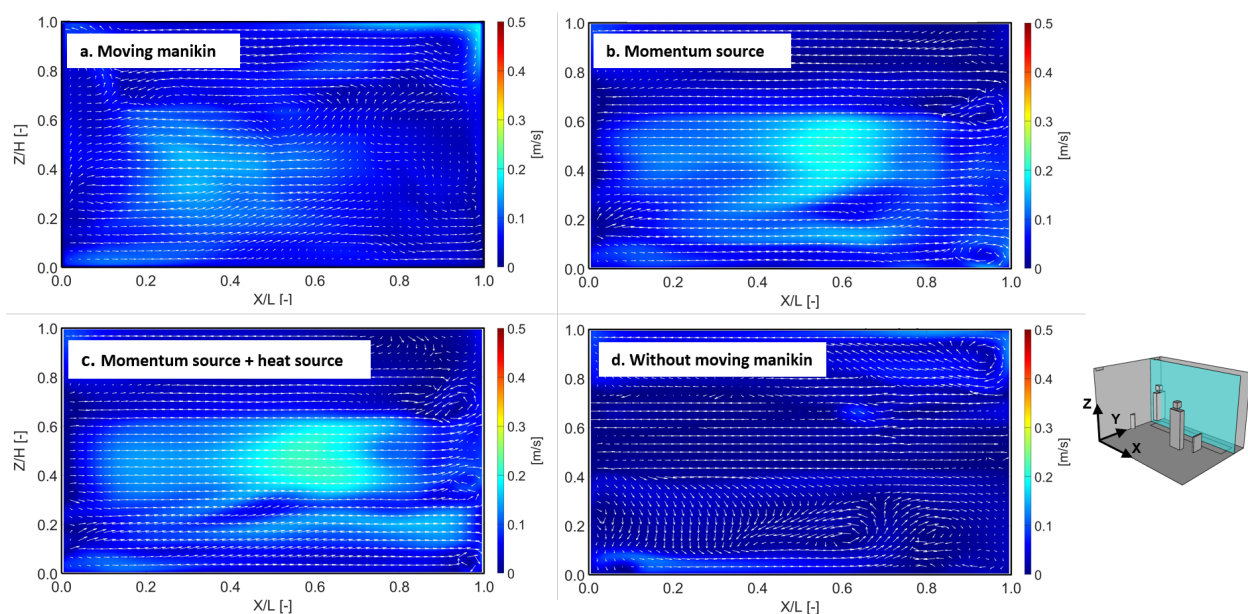

Figure 23. Comparison of velocity magnitude and velocity vector in the vertical central plane of the moving zone.
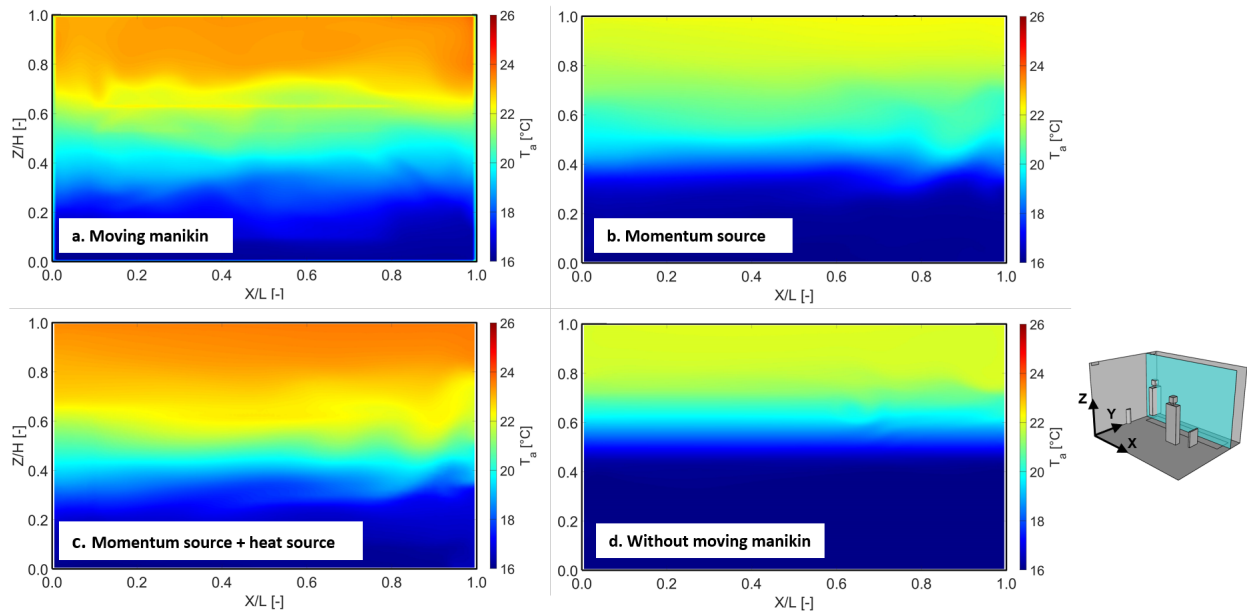
Title
Progress report

Version
1.0

Page
32 of 41

Figure 24. Comparison of air temperature in the middle plane of target manikin in the vertical central plane of the moving zone.

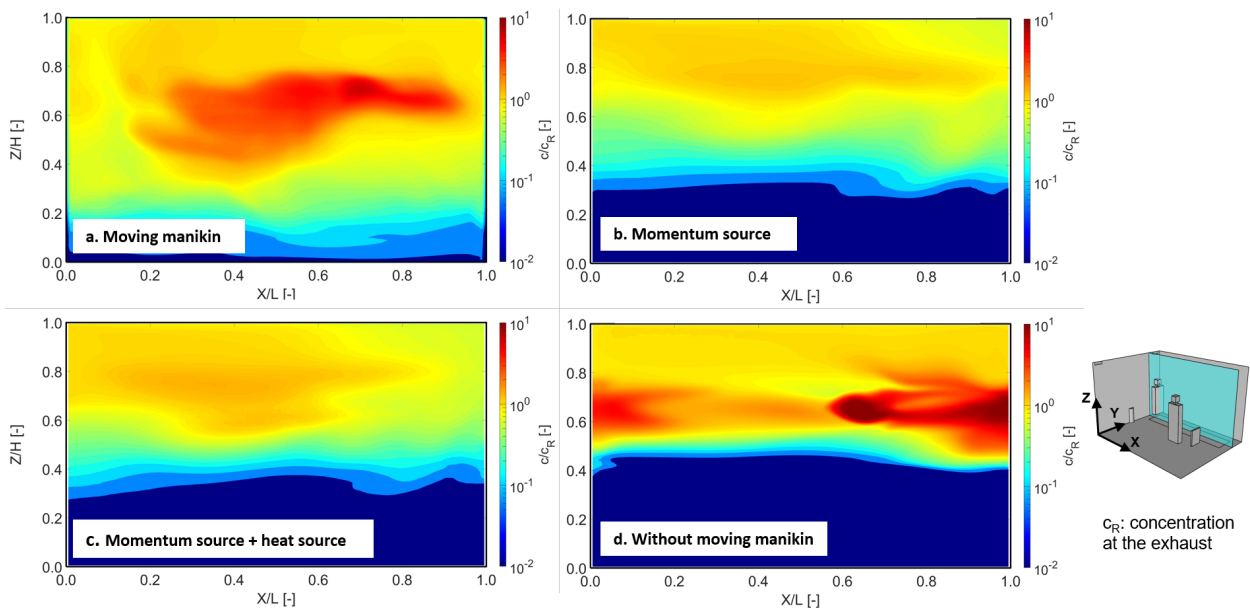**Figure 25.** Comparison of dimensionless concentration in the vertical central plane of the moving zone for PM1 ($d_p = 1$ μm).

5.4.2. Horizontal plane at the mouth height

At the mouth height, the velocity distributions present a significant difference between the overset mesh method and the momentum source method, as shown in Figure 26. When using a source term in the moving zone, the flow pattern is dominated by a large recirculation in the plane of the mouth height. In most regions, the air speeds are higher than those in the case a of overset mesh method. Without human movement, the air speed at the mouth height is very low (Figure 26d). Compared to the influence of the

Title
Progress report

Version
1.0

Page
33 of 41

momentum source on the velocity distributions, the influence of the heat source on the flow pattern is minimal.

Figure 27 compares the air temperature distribution in the horizontal plane of mouth height. Under displacement ventilation, the thermal stratification is pronounced in this room, as shown in Figure 24. Therefore, the air temperature at the mouth height is affected by the strength of thermal stratification. In this plane, the air temperature obtained with a heat source in the moving zone (case c) is slightly higher than that from the explicit modeling method (case a), which may be attributed to the increased mixing above the interface height, as developed from the displacement ventilation, by adding a momentum source. Without a heat source, the air temperatures in this plane are around one (case b) or two (case d) degrees lower than those with explicitly modeled moving manikin (case a).

Figure 28 compares the concentration distribution in the horizontal plane of mouth height. The significant differences in the distribution of air velocity result in a pronounced difference in particle concentration distribution. The particle dispersion is locked by the primary recirculation in this plane when using a momentum source (Figure 28b and Figure 28c). Therefore, the particle concentration is high near the source manikin, and the particle concentration is relatively low near the wall surfaces. Due to the enhancement of air mixing from human movement, particle concentration distribution tends to be more uniform in case a with explicitly modeled moving manikin (Figure 28a).
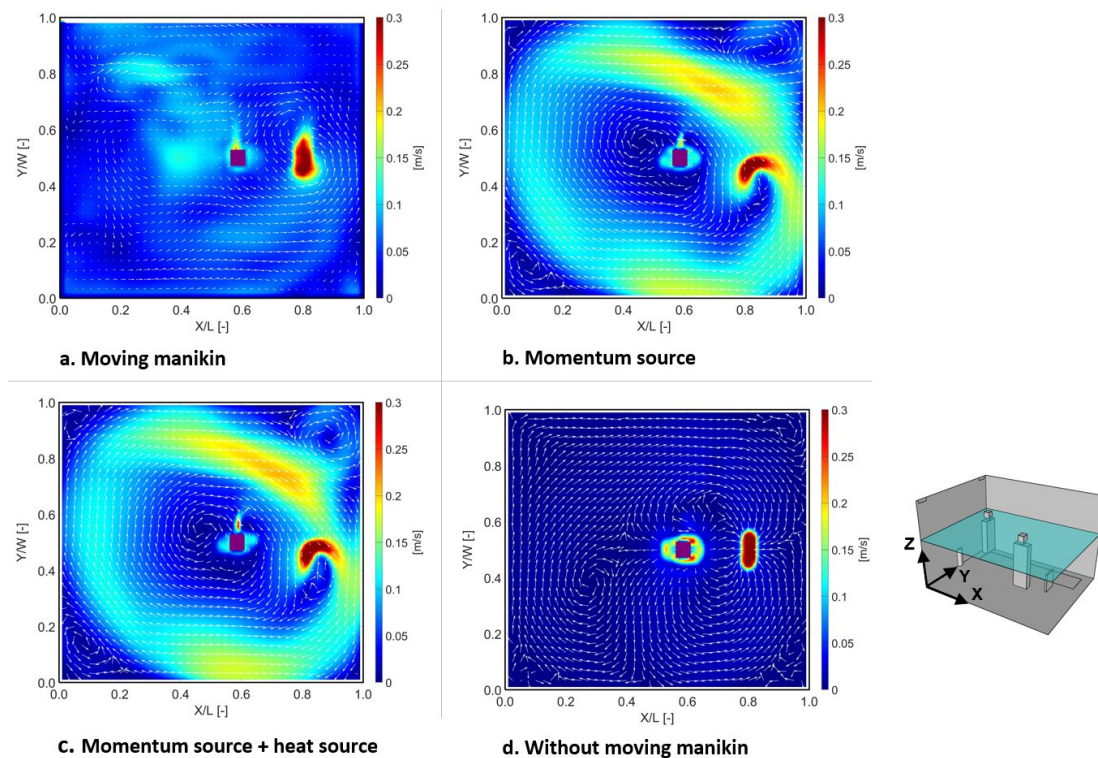

Figure 26. Comparison of velocity magnitude and velocity vector in the horizontal plane of the mouth height.
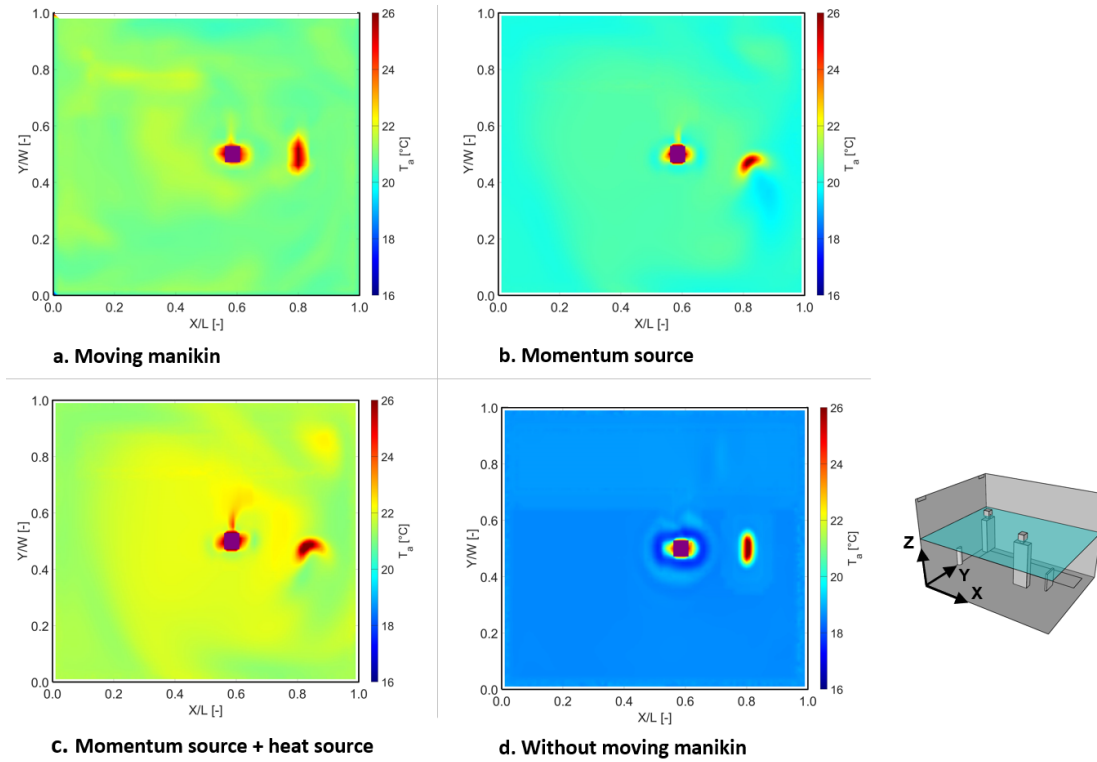
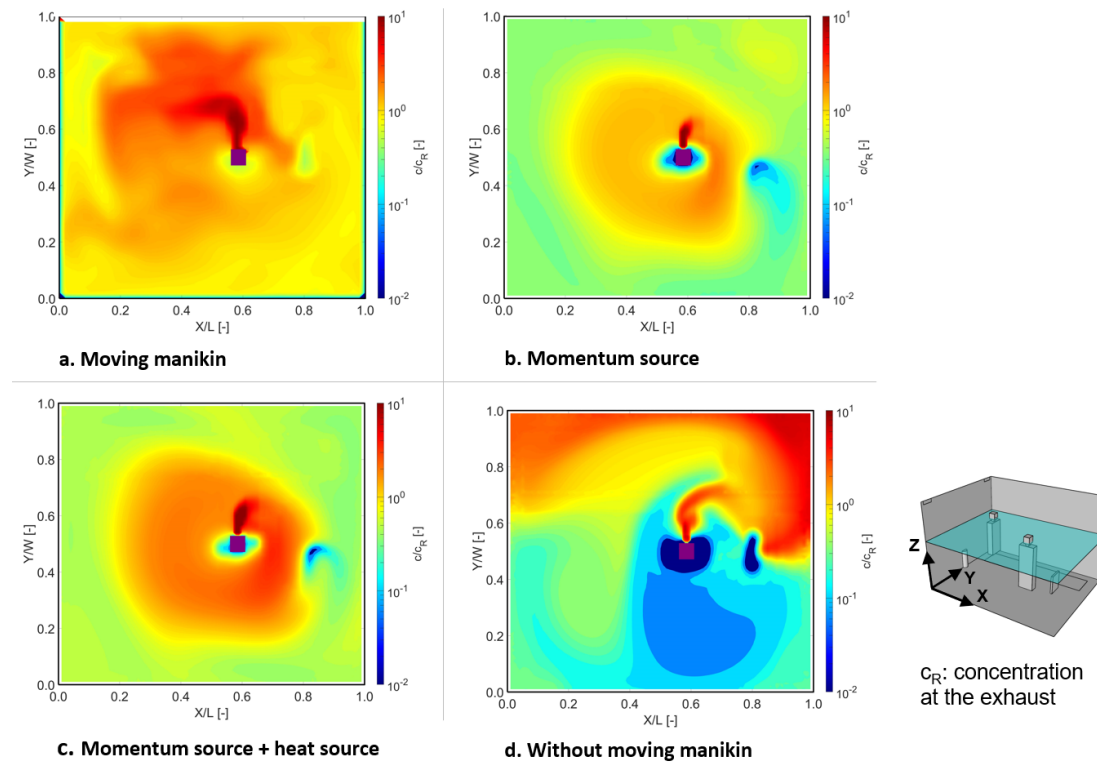**Figure 27.** Comparison of air temperature in the horizontal plane of the mouth height.

Figure 28. Comparison of dimensionless concentration of PM1 in the horizontal plane of the mouth height.

Title
Progress report

Version
1.0

Page
35 of 41

5.4.3. Exposure index at the breathing zone

The exposure indexes at the breathing zone from Equation 3 are calculated and compared to assess the individual exposure from different modeling methods of human movement. Figure 29a shows the time evolution history of exposure index at the breathing zone with explicitly modeled moving manikin., The breathing zone herein is defined as a cubic area with a dimension of 100 mm near the mouth and nose of the moving manikin (exposed person). As shown in Figure 29a, the exposure indexes are nearly identical for particle sizes equal to or smaller than 2 μm. For particles with larger sizes (PM5 and PM10), the particle concentration at the exhaust is smaller due to particle deposition to the wall surfaces, resulting in higher exposure indexes during human movement. The exposure indexes first increase after the starting of human movement, then reach the highest level during the period of 5 s to 7 s, and finally decrease afterward to the lowest level till the time around 10 s. In the period of 10 s to 15 s, the exposure indexes are close to those of the starting time.

Small spikes are observed in Figure 29a for the dynamic exposure indexes. Figure 16b in Section 5.1 showed that the cell size is not comparable between the background grid and the moving component grid. In addition, the time step size used in the transient simulation is small (0.01 s). Therefore, in the transient simulations with overset mesh, there are times when cell size is very small for the overset mesh near the boundaries of moving manikin, which is not good for data exchange and leads to some strange data locally, as shown previously in Figure 19 at the time of 5.4 s and 7.2 s. This thus causes spikes in the dynamic exposure indexes at the breathing zone.

Figure 29b shows the time-average or average results of exposure indexes in the breathing zone for the four simulation cases. The breathing zone herein is defined as a region in the moving zone with a dimension of 100 mm in height near the mouth and nose. The height of the defined breathing zone is between 1.5 m to 1.6 m above the floor surface. The average exposure indexes between case a (moving manikin) and case d (without moving manikin) are relatively close. For smaller particles (d ≤ 5 μm), the exposure indexes obtained without moving manikin (case d) are around 10% or 20% smaller than the first case with explicitly modeled moving manikin. For PM10, the average exposure index from case d is larger than from case a. When the momentum source is added to the moving zone (cases b and c), a stable flow pattern forms in the breathing zone, as shown in Figure 26. The large recirculation at the breathing height leads to lower particle concentration in the breathing zone of the target manikin, as shown in Figure 28. Therefore, exposure indexes are smaller in cases 2 and 3 than in the other two cases.
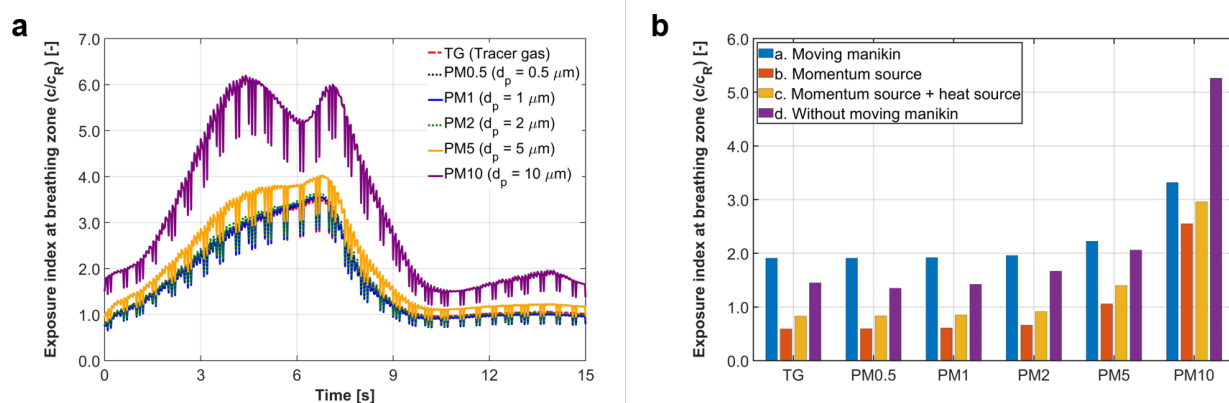

Figure 29. Exposure index at the breathing zone. (a) Time evolution history of the explicitly modeled moving manikin; (b) (time-)averaged results in the moving zone.

6. Discussions and suggestions

- It is recognized that the Eulerian or Lagrangian approach has its own merits and limitations. The drift-flux model of the Eulerian approach, in which the settling flux and deposition flux are taken into account, can predict the airborne transmission of fine particles with reasonable accuracy. To reduce calculation and post-processing time, the Eulerian approach (drift-flux model) can be used. On the other hand, if the trajectories of particles are of interest, the Lagrangian approach is a better choice.

- In the simulations, to a large extent, the steady breathing mode (exhalation for source manikin and inhalation for target manikin) reproduces the expiratory particle dispersion in the room as obtained from the transient breathing mode in the logarithmic scale. However, the simulation results from a steady exhalation boundary at the mouth for the target manikin deviates significantly from the transient breathing mode. When performing CFD simulation by steady breathing mode, an average mouth velocity from the pulmonary ventilation rate underestimates the particle dispersion released by the source manikin, resulting in lower exposure indexes at the target manikin. A proper selection of the steady mouth velocity and velocity direction will need to be investigated in further studies.

- When modeling human movement, the average exposure indexes are similar between the modeling case for explicitly modeled manikin and the case without moving manikin, indicating that the influence of the human movement on the individual exposure is limited in the investigated configuration with a moving speed of 0.2 m/s. However, a higher moving speed might have a stronger effect on individual exposure, which can be investigated in future studies. In addition, human movement in residential spaces is usually a short-term event with an order of magnitude in seconds or minutes. Within less than a minute the velocity flow field can recover to its steady-state situation. The reversion of the concentration conditions to the steady-state situation is a function of the air change rate and (local) air change efficiency, which is also not very long when the ventilation rate is high. Therefore, the influence of short-term human movement is also limited in the long term.

- Through the comparison discussed in Section 5.4, it is found that a fixed source term added to the whole moving zone cannot fully reproduce the particle dispersion during human movement. A time-dependent source term or distributed source term can be a better solution to modeling human movement when using a simplified method.

7. Conclusions

The sub-studies show that it is not straightforward to model the spread of pathogens in a room. Simplifications are possible, but one should be aware of the assumptions made when analyzing. On the other hand, the application of complex modeling techniques may assume a better agreement with reality, but the information required for modeling may not be at the level available, and the number of parameters that need assumptions increases. In that case, it may be better to keep the approach simpler with a similar quality outcome.

From the three studies, we conclude that the following approaches should be pursued for the remainder of CFD studies performed within P3Venti:

- Simulation of the spread of pathogens (particles, aerosols) is best performed via the application of the drift-flux model. For very small particles (<5 μm) the difference with a scalar approach is limited. For larger particles, the effect of gravitation may affect the distribution significantly. This depends on the type of airflow in the room. Application of the drift-flux model will ensure that, in any case, the gravitational effect is included. Lagrangian particle tracking may provide more accurate particle concentration distribution, but not all forces can be well defined, and the time needed for such simulations would hamper the number of cases that can be simulated.

- The breathing of a person (exhalation of pathogens) may be assumed with constant airflow, reflecting the average momentum for exhalation. However, care should be taken on a proper selection of boundary conditions of exhalation and inhalation jets. The exhalation jet at the highest velocity level may not be well modeled in this case, but we may assume that, in reality, exhalation will not be perfectly sinusoidal

and that nose exhalation will also take place. Mouth exhalation, as proposed, will present a (nearly) worst-case scenario.

- Modeling movement/disturbances affect the flow field and, in some instances, will affect the exposure to pathogens. However, the modeling of movement via dynamic meshing is not feasible. The alternative solution via a momentum (and heat) source can capture the extra disturbance caused by the movement to a certain extent. The need for modeling of movement/disturbances should be considered well for each case as one may assume that exposure will predominantly take place in a steady-state mode for many situations and instances.

References

Ai, Z.T., Hashimoto, K., Melikov, A.K., 2019. Airborne transmission between room occupants during short-term events: Measurement and evaluation. Indoor Air 29, 563-576. https://doi.org/10.1111/ina.12557

Ai, Z.T., Melikov, A.K., 2018. Airborne spread of expiratory droplet nuclei between the occupants of indoor environments: A review. Indoor Air 28, 500-524. https://doi.org/10.1111/ina.12465

Al Assaad, D., Ghali, K., Ghaddar, N., 2019. Effect of flow disturbance induced by walking on the performance of personalized ventilation coupled with mixing ventilation. Build. Environ. 160, 106217. https://doi.org/10.1016/j.buildenv.2019.106217

Asadi, S., Wexler, A.S., Cappa, C.D., Barreda, S., Bouvier, N.M., Ristenpart, W.D., 2019. Aerosol emission and superemission during human speech increase with voice loudness. Sci. Rep. 9. https://doi.org/10.1038/s41598-019-38808-z

Bjørn, E., Nielsen, P. V., 2002. Dispersal of exhaled air and personal exposure in displacement ventilated rooms. Indoor Air 12, 147-164. https://doi.org/10.1034/j.1600-0668.2002.08126.x

Brohus, H., Balling, K.D., Jeppesen, D., 2006. Influence of movements on contaminant transport in an operating room. Indoor Air 16, 356-372. https://doi.org/10.1111/j.1600-0668.2006.00454.x

Brohus, H., Balling, K.D., Jeppesen, D., 2008. Influence of movements on contaminant transport in an operating room, in: The 11 Th International Conference on Indoor Air Quality and Climate. https://doi.org/10.1111/j.1600-0668.2006.00454.x

Cao, G., Awbi, H., Yao, R., Fan, Y., Sirén, K., Kosonen, R., Zhang, J. (Jensen), 2014. A review of the performance of different ventilation and airflow distribution systems in buildings. Build. Environ. https://doi.org/10.1016/j.buildenv.2013.12.009

Cao, S.J., Cen, D., Zhang, W., Feng, Z., 2017. Study on the impacts of human walking on indoor particles dispersion using momentum theory method. Build. Environ. 126, 195-206. https://doi.org/10.1016/j.buildenv.2017.10.001

Cermak, R., Melikov, A.K., 2007. Protection of occupants from exhaled infectious agents and floor material emissions in rooms with personalized and underfloor ventilation. HVAC R Res. 13, 23-38. https://doi.org/10.1080/10789669.2007.10390942

Chen, C., Zhao, B., 2010. Some questions on dispersion of human exhaled droplets in ventilation room: Answers from numerical investigation. Indoor Air 20, 95-111. https://doi.org/10.1111/j.1600-0668.2009.00626.x

Chen, F., Yu, S.C.M., Lai, A.C.K., 2006. Modeling particle distribution and deposition in indoor environments with a new drift-flux model. Atmos. Environ. 40, 357-367. https://doi.org/10.1016/j.atmosenv.2005.09.044

Choi, J.I., Edwards, J.R., 2008. Large eddy simulation and zonal modeling of human-induced contaminant transport. Indoor Air 18, 233-249. https://doi.org/10.1111/j.1600-0668.2008.00527.x

Edge, B.A., Paterson, E.G., Settles, G.S., 2005. Computational study of the wake and contaminant transport of a walking human. J. Fluids Eng. Trans. ASME 127, 967-977. https://doi.org/10.1115/1.2013291

Eslami, J., Abbassi, A., Saidi, M.H., 2017. Numerical simulation of the effect of visitor's movement on bacteria-carrying particles distribution in hospital isolation room. Sci. Iran. 24, 1160-1170. https://doi.org/10.24200/sci.2017.4097

Finlay, W.H., 2001. The mechanics of inhaled pharmaceutical aerosols: an introduction. Academic press.

Gao, N.P., Niu, J.L., 2007. Modeling particle dispersion and deposition in indoor environments. Atmos. Environ. 41, 3862-3876. https://doi.org/10.1016/j.atmosenv.2007.01.016

Gupta, J.K., Lin, C.H., Chen, Q., 2010. Characterizing exhaled airflow from breathing and talking. Indoor Air 20, 31-39. https://doi.org/10.1111/j.1600-0668.2009.00623.x

Han, Z., Sze To, G.N., Fu, S.C., Chao, C.Y.H., Weng, W., Huang, Q., 2014. Effect of human movement on airborne disease transmission in an airplane cabin: Study using numerical modeling and quantitative risk analysis. BMC Infect. Dis. 14, 1-19. https://doi.org/10.1186/1471-2334-14-434/FIGURES/11

Holmberg, S., Chen, Q., 2003. Air flow and particle control with different ventilation systems in a classroom. Indoor Air 13, 200-204. https://doi.org/10.1034/j.1600-0668.2003.00186.x

Johnson, G.R., Morawska, L., 2009. The mechanism of breath aerosol formation. J. Aerosol Med. Pulm. Drug Deliv. 22, 229-237. https://doi.org/10.1089/jamp.2008.0720

Lai, A.C.K., Nazaroff, W.W., 2000. Modeling indoor particle deposition from turbulent flow onto smooth surfaces. J. Aerosol Sci. 31, 463-476. https://doi.org/10.1016/S0021-8502(99)00536-4

Lai, A.C.K., Chen, F.Z., 2007. Comparison of a new Eulerian model with a modified Lagrangian approach for particle distribution and deposition indoors. Atmos. Environ. 41, 5249-5256. https://doi.org/10.1016/j.atmosenv.2006.05.088

Li, X., Ai, Z., Ye, J., Mak, C.M., Wong, H.M., 2022a. Airborne transmission during short-term events: Direct route over indirect route. Build. Simul. 1-14. https://doi.org/10.1007/s12273-022-0917-9

Li, X., Mak, C.M., Ai, Z., Wong, H.M., 2022b. Airborne transmission of exhaled pollutants during short-term events: Quantitatively assessing inhalation monitor points. Build. Environ. 223, 109487. https://doi.org/10.1016/j.buildenv.2022.109487

Li, C., Wang, H., Yu, C.W., Xie, D., 2022c. Diffusion characteristics of the industrial submicron particle under Brownian motion and turbulent diffusion. Indoor Built Environ. 31, 17–30. https://doi.org/10.1177/1420326X21991055

Lipczynska, A., Kaczmarczyk, J., Melikov, A.K., 2015. Thermal environment and air quality in office with personalized ventilation combined with chilled ceiling. Build. Environ. 92, 603-614. https://doi.org/10.1016/J.BUILDENV.2015.05.035

Mei, S.J., Hu, J.T., Liu, D., Zhao, F.Y., Li, Y., Wang, H.Q., 2019. Airborne pollutant dilution inside the deep street canyons subjecting to thermal buoyancy driven flows: Effects of representative urban skylines. Build. Environ. 149, 592-606. https://doi.org/10.1016/j.buildenv.2018.12.050

Menter, F.R., 1994. Two-equation eddy-viscosity turbulence models for engineering applications. AIAA J. 32, 1598-1605. https://doi.org/10.2514/3.12149

Morawska, L., Johnson, G.R., Ristovski, Z.D., Hargreaves, M., Mengersen, K., Corbett, S., Chao, C.Y.H., Li, Y., Katoshevski, D., 2009. Size distribution and sites of origin of droplets expelled from the human respiratory tract during expiratory activities. J. Aerosol Sci. 40, 256-269. https://doi.org/10.1016/j.jaerosci.2008.11.002

Murakami, S., Kato, S., Nagano, S., Tanaka, Y., 1992. Diffusion characteristics of airborne particles with gravitational settling in a convection-dominant indoor flow field, ASHRAE Transactions.

Nazaroff, W.W., 2008. Inhalation intake fraction of pollutants from episodic indoor emissions. Build. Environ. 43, 269-277. https://doi.org/10.1016/j.buildenv.2006.03.021

Nazaroff, W.W., 2022. Indoor aerosol science aspects of SARS-CoV-2 transmission. Indoor Air 32, e12970. https://doi.org/10.1111/ina.12970

Olmedo, I., Nielsen, P. V., Ruiz de Adana, M., Jensen, R.L., Grzelecki, P., 2012. Distribution of exhaled contaminants and personal exposure in a room using three different air distribution strategies. Indoor Air 22, 64-76. https://doi.org/10.1111/j.1600-0668.2011.00736.x

Olmedo, I., Nielsen, P. V., de Adana, M.R., Jensen, R.L., 2013. The risk of airborne cross-infection in a room with vertical low-velocity ventilation. Indoor Air 23, 62-73. https://doi.org/10.1111/j.1600-0668.2012.00794.x

Qian, H., Li, Y., Nielsen, P. V., Hyldgaard, C.E., Wong, T.W., Chwang, A.T.Y., 2006. Dispersion of exhaled droplet nuclei in a two-bed hospital ward with three different ventilation systems. Indoor Air 16, 111-128. https://doi.org/10.1111/J.1600-0668.2005.00407.X

Ren, C., Feng, Z., Cen, D., Cao, S.J., 2019. Study on the subway environment induced by moving train using Gaussian distributed momentum source theory method. Indoor Built Environ. 28, 1083-1091. https://doi.org/10.1177/1420326X18820473

Sheikhnejad, Y., Aghamolaei, R., Fallahpour, M., Motamedi, H., Moshfeghi, M., Mirzaei, P.A., Bordbar, H., 2022. Airborne and Aerosol Pathogen Transmission Modeling of Respiratory Events in Buildings: An Overview of Computational Fluid Dynamics. Sustain. Cities Soc. 103704. https://doi.org/10.1016/j.scs.2022.103704

Sze To, G.N., Chao, C.Y.H., 2010. Review and comparison between the Wells-Riley and dose-response approaches to risk assessment of infectious respiratory diseases. Indoor Air. https://doi.org/10.1111/j.1600-0668.2009.00621.x

Villafruela, José Manuel, Castro, F., San José, J.F., Saint-Martin, J., 2013a. Comparison of air change efficiency, contaminant removal effectiveness and infection risk as IAQ indices in isolation rooms. Energy Build. 57, 210-219. https://doi.org/10.1016/j.enbuild.2012.10.053

Villafruela, J. M., Olmedo, I., Ruiz de Adana, M., Méndez, C., Nielsen, P. V., 2013b. CFD analysis of the human exhalation flow using different boundary conditions and ventilation strategies. Build. Environ. 62, 191-200. https://doi.org/10.1016/j.buildenv.2013.01.022

Villafruela, J.M., Olmedo, I., San José, J.F., 2016. Influence of human breathing modes on airborne cross infection risk. Build. Environ. 106, 340-351. https://doi.org/10.1016/j.buildenv.2016.07.005

Wang, J., Chow, T.T., 2011. Numerical investigation of influence of human walking on dispersion and deposition of expiratory droplets in airborne infection isolation room. Build. Environ. 46, 1993-2002. https://doi.org/10.1016/j.buildenv.2011.04.008

Yakhot, V., Orszag, S.A., Thangam, S., Gatski, T.B., Speziale, C.G., 1992. Development of turbulence models for shear flows by a double expansion technique. Phys. Fluids 4, 1510-1520. https://doi.org/10.1063/1.858424

Yang, J., Sekhar, S.C., Cheong, K.W.D., Raphael, B., 2015. Performance evaluation of a novel personalized ventilation-personalized exhaust system for airborne infection control. Indoor Air 25, 176-187. https://doi.org/10.1111/INA.12127

Z. Warhaft, 2000. Passive Scalars in Turbulent Flows. Annu. Rev. Fluid Mech. 32, 203-240.

Zhang, Z., Chen, Q., 2007. Comparison of the Eulerian and Lagrangian methods for predicting particle transport in enclosed spaces. Atmos. Environ. 41, 5236-5248. https://doi.org/10.1016/j.atmosenv.2006.05.086

Zhao, B., Li, X., Zhang, Z., 2004a. Numerical study of particle deposition in two differently ventilated rooms. Indoor Built Environ. 13, 443-451. https://doi.org/10.1177/1420326X04048729

Zhao, B., Zhang, Y., Li, X., Yang, X., Huang, D., 2004b. Comparison of indoor aerosol particle concentration and deposition in different ventilated rooms by numerical method. Build. Environ. 39, 1-8. https://doi.org/10.1016/j.buildenv.2003.08.002

Zhao, B., Zhang, Z., Li, X., Huang, D., 2004c. Comparison of diffusion characteristics of aerosol particles in different ventilated rooms by numerical method. ASHRAE Trans. 110, 88-95.

Zhao, B., Yang, C., Yang, X., Liu, S., 2008. Particle dispersion and deposition in ventilated rooms: Testing and evaluation of different Eulerian and Lagrangian models. Build. Environ. 43, 388-397. https://doi.org/10.1016/j.buildenv.2007.01.005

Title
Progress report

Version
1.0

Page
41 of 41